Title (116 symbols): Astrocytic PIEZO activation by heartbeat sound promotes extracellular matrix and maturation in human brain organoids

Title (90 symbols): Astrocytic PIEZO activation by heartbeat sound promotes ECM synthesis and neurodevelopment

Short title: Heartbeat promotes ECM via PIEZO

Alexandra Ferreira Oliveira[1], Florian Rambow[2], Samira Makhzami[2], Yury A. Nikolaev[3], Angelo Novak[4], Olga Shevchuk[4], Hannah Voss[4], Daniel R. Engel[4], Paul A. Schult[1], Matthias Pillath-Eilers[1], Britta Kaltwasser[1], Ulf Brockmeier[1], Christoph Kleinschnitz[1], Dirk M. Hermann[1] and Egor Dzyubenko[1,*]

[1] Department of Neurology and Center for Translational Neuro- and Behavioral Sciences (C-TNBS), University Hospital Essen, Hufelandstraße 55, Essen D-45122, Germany
[2] Department of Applied Computational Cancer Research, Institute for AI in Medicine (IKIM), University Hospital Essen, Girardetstraße 2, D45131 Essen, Germany
[3] Faculty of Medicine, Medical and Translational Biology, Umeå University, Universums gränd 4, SE-90187 Umeå, Sweden
[4] Institute for Experimental Immunology and Imaging, Department Immunodynamics, University Hospital Essen, Hufelandstraße 55, Essen D-45122, Germany

[*] **Corresponding author:**
PD Dr. Egor Dzyubenko, Department of Neurology and Center for Translational Neuro- and Behavioral Sciences (C-TNBS), University Hospital Essen, Hufelandstraße 55, Essen D-45122, Germany. Email: egor.dzyubenko@uk-essen.de

Word count (Abstract):	177
Word count (main text and figure legends):	3024
Word count (Methods):	3113
Figures:	4
Tables:	2
Supplementary Figures:	13
Supplementary Tables:	2
References:	47

Conflict of interest disclosure: The authors have no competing interests related to this work

Ethics approval: Experimental procedures were approved by the local government (Landesamt für Natur, Umwelt und Verbraucherschutz, Recklinghausen) and conducted in accordance with European Union directive 2010/63/EU and local institutional guidelines

Abstract:

Heartbeat sound is one of the first rhythmic stimuli encountered by the developing human brain, yet its biological role has remained unexplored. Here we show that heartbeat sound promotes structural and functional maturation of human cortical organoids with a physiological astrocyte-to-neuron ratio. Continuous stimulation with heartbeat expanded the extracellular space (ECS), visualized by super-resolution 3D STED and 2-photon shadow imaging, and increased extracellular matrix (ECM) synthesis, detected by LC-MS/MS proteomics. Heartbeat sound promoted neuronal and astrocytic differentiation, synaptogenesis, and organoid maturation, as shown by single-cell RNA sequencing, synaptic marker immunohistochemistry, and high-density multielectrode electrophysiology. Transcriptomic analyses demonstrated astrocyte-specific expression of mechanosensitive PIEZO channels. Using Ca^{2+} imaging, we confirmed that low-frequency sound stimulation, including heartbeat, activates PIEZO-mediated Ca^{2+} responses, which in turn upregulate astrocytic ECM synthesis. Experiments with biomimetic hydrogels demonstrated that physiological matrix stiffness attenuates PIEZO activation, suggesting a mechanoprotective mechanism. Our findings demonstrate a fundamental mechanism for inducing ECM synthesis and neural differentiation through astrocytic PIEZO activation by heartbeat sound, suggesting that interoception of the internal acoustic environment is an underappreciated driver of human brain development.

Keywords: mechanoreceptor, neuron-glia interactions, extracellular matrix, extracellular space, cortical organoid, neurodevelopment

Highlights

- Heartbeat sound activates PIEZO ion channels
- Astrocytic PIEZO activation promotes extracellular matrix synthesis
- Heartbeat sound stimulates neural differentiation and brain organoid maturation

65 **Graphical Abstract**

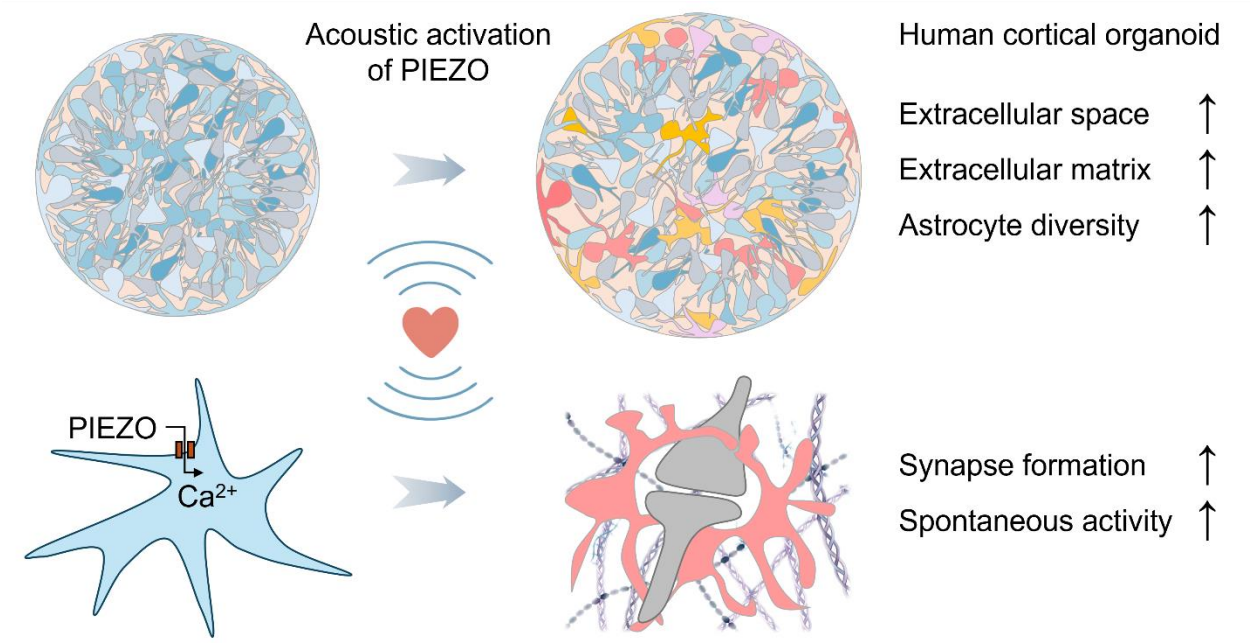

66

67

68

Introduction

Mother's heartbeat is one of the first sounds that a human fetus hears starting the third trimester of pregnancy (Querleu et al., 1988). Yet, even before the auditory system fully develops, the embryo is exposed to acoustic stimulation, which is dominated by sound frequencies below 200 Hz including those elicited by maternal heartbeat (Dealessandri and Vivalda, 2018; Vince et al., 1982). While the high frequencies are strongly attenuated inside the womb, low frequency sounds can be as loud as 100 dB (Dealessandri and Vivalda, 2018; Gerhardt et al., 1990). Therefore, the acoustic environment of an embryo is defined by low-frequency sound waves generating persistent mechanical oscillations that rhythmically stimulate developing tissues.

In mammalian tissues, mechanical oscillations are mainly detected by PIEZO ion channels (Coste et al., 2010; Zhao et al., 2018), which have been implicated in interoceptive regulation of breathing (Tort et al., 2025) and blood pressure (Jammal Salameh et al., 2024; Zeng et al., 2018). PIEZO1 and PIEZO2 are mechanically activated ion channels that share a common activation mechanism gated by membrane tension. While PIEZO2 is predominantly expressed by somatosensory neurons, PIEZO1 is also found in glial (Chi et al., 2022), vascular (Ranade et al., 2014), and immune cells (Solis et al., 2019).

The molecular mechanisms of sound-driven mechanotransduction remain underinvestigated. Although the possibility of inducing cellular responses by sound stimulation has been demonstrated (Kumeta et al., 2025; Xu et al., 2024), the physiological relevance and mechanistic understanding of such stimulation has remained elusive. We hypothesized that heartbeat sound provides a natural mechanical stimulus that shapes embryonic brain development.

For experimental studies of human neurodevelopment, brain organoids derived from human induced pluripotent stem cells (hiPSCs) have become the model of choice. Originally designed to recapitulate cortical organization (Lancaster et al., 2013) and to model developmental disorders, organoid systems have since been adapted to study interactions between brain regions and to investigate connectivity-related diseases such as epilepsy (Onesto et al., 2024). Despite these advances, current organoid models do not capture the acoustic environment during early brain development. In this study, we investigated how mechanostimulation with heartbeat sound shapes cellular physiology and functional maturation in human cortical organoids, focusing on the brain extracellular matrix (ECM), neural cell differentiation, synaptogenesis, and neuronal activity.

Results

Heartbeat sound expands the extracellular space in astrocyte-enriched organoids

Astrocyte-enriched cortical organoids were generated by co-culturing neural precursor cells (NPCs) with induced astrocytes (iAstrocytes) using a modified growth factor-based protocol (Paşca et al., 2015) (**Fig. 1A**). By day 45, they developed ramified astrocytes, glutamatergic synapses, and showed increased ECM expression compared with non-enriched cortical organoids (Fig. S1). Cortical organoids with and without astrocyte enrichment were exposed to a human heartbeat audio recording for 31 days of maturation, with ambient noise as control. Hydrophone measurements in cultivation medium (**Fig. 1B**) were used to tune the applied heartbeat sound to physiological acoustic environment of an embryo during gestation (Table 1).

Heartbeat sound increased the extracellular space (ECS) volume fraction in astrocyte-enriched organoids by 39% (23.4±3.5 vs 16.8±6.2 %, mean±SD) (**Fig. 1C, C'**), shown by 3D STED superresolution shadow imaging (SuSHi) (Tonnesen et al., 2018), explained in (Fig. S2). This observation was confirmed with 2-photon (2P) shadow imaging indicating a 31% (33.1±5.6 vs 25.2±5.8 %, mean±SD) ECS volume increase in astrocyte-enriched organoids stimulated with heartbeat sound (**Fig. 1D, D'**). Higher ECS volume fractions measured with 2P are due to lower resolution compared with 3D STED (Table S1) and consequent under-detection of small cellular structures. No major changes in the ECS volume were observed in organoids without astrocyte enrichment (Fig. S3).

Heartbeat sound promotes ECM synthesis in astrocyte-enriched organoids

Because the expanded ECS needs to be stabilized by an extracellular scaffold to maintain tissue integrity and diffusion (Tønnesen et al., 2023), we next analyzed protein expression using LC-MS/MS. Gene Ontology Cellular Component (GOCC) enrichment analysis comparing heartbeat-stimulated and control organoids revealed ECM among the top regulated terms (**Fig. 1E)**. In astrocyte-enriched organoids, heartbeat sound stimulation upregulated multiple ECM scaffolding proteins, among them fibronectin (FN1) and vitronectin (VTN), and synapse organizing molecules including glypican 4 (GPC4), neuroligins (NLGN1, NLGN2), and plexin-B (PLXNB1) (**Fig. 1F** and Fig. S4**).** In organoids without astrocyte enrichment, we found no major changes in ECM expression following heartbeat sound stimulation (Fig. S4).

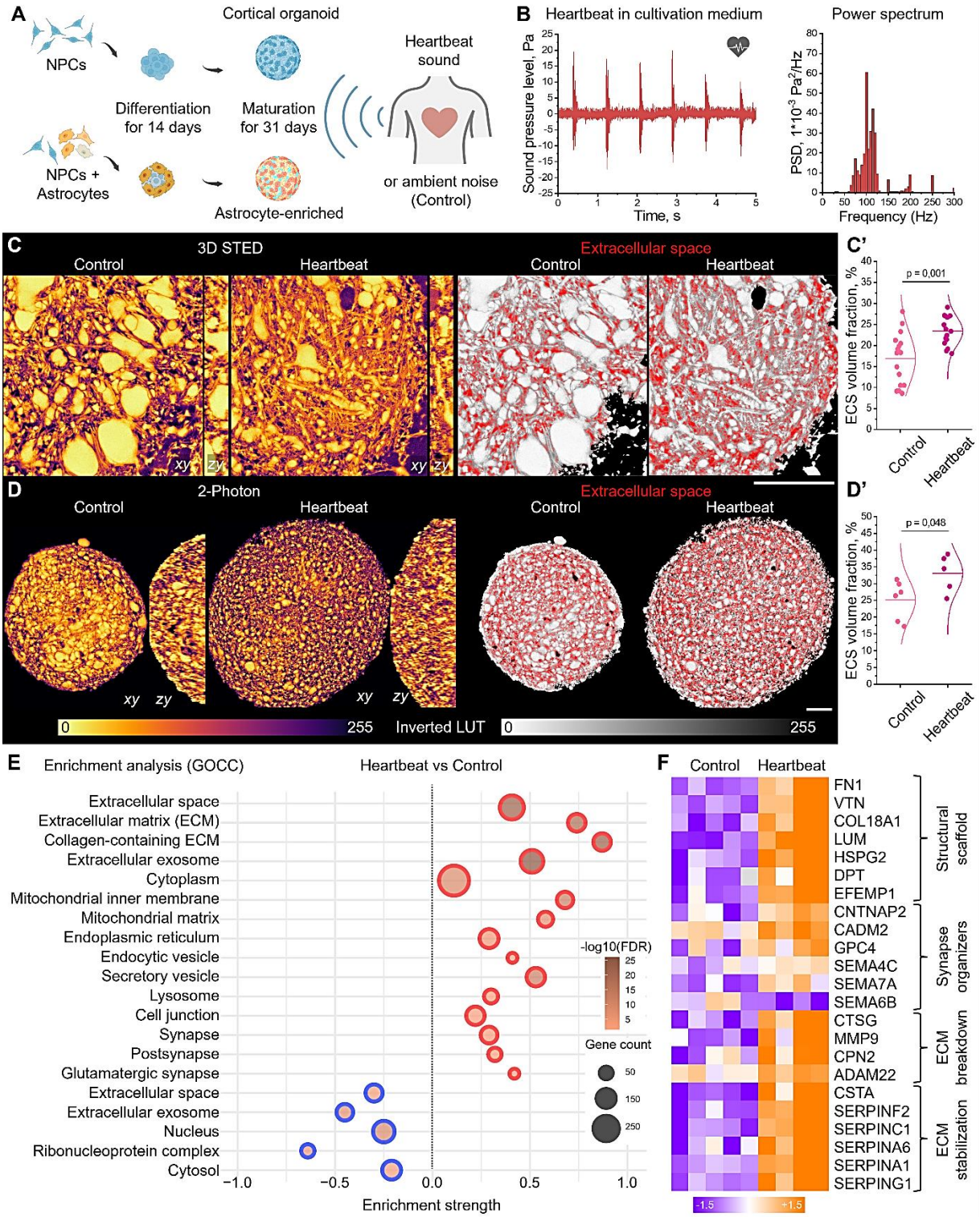

Figure 1. Stimulation with heartbeat sound increases ECS volume and ECM expression in astrocyte-enriched human cortical organoids. (**A**) Generation of organoids and exposure to heartbeat. (**B**) Hydrophone recording and power spectrum of the applied heartbeat sound in cultivation medium. (**C**) Superresolution 3D STED shadow imaging and ECS segmentation (red) in live organoids. (**C'**) ECS volume fraction comparison, t-test (n=10-15). (**D**) 2P shadow imaging and ECS segmentation (red) in live

organoids. (**D'**) ECS volume fraction comparison, t-test (n=5-6). (**C**, **D**) Images are xy and zy projections; LUT inverted (see Fig S2 for details). Scale bars, 50 µm. (**E**) Gene ontology cellular component (GOCC) enrichment analysis of protein expression in heartbeat-stimulated vs control astrocyte-enriched organoids, based on significantly regulated proteins ($p < 0.05$, fold change difference > 1.5, t-test), measured by LC-MS/MS. (**F**) Heatmap shows normalized, centered (mean subtraction) log2 protein abundances of selected ECM proteins regulated by heartbeat sound. Other regulated ECM proteins are shown in Fig S4.

Heartbeat sound promotes neural differentiation in astrocyte-enriched organoids

The brain ECM is jointly produced by neurons and glial cells, forming a dynamic scaffold that controls cell differentiation and neuroplasticity (Dzyubenko and Hermann, 2023; Faissner and Reinhard, 2015). To examine cellular composition and phenotypic changes induced by heartbeat sound, we performed single-cell RNA sequencing (scRNAseq). In astrocyte-enriched organoids, heartbeat sound stimulation increased glutamatergic neuron differentiation (23.7 % vs 13.5 % of total cell counts, heartbeat vs control) (**Fig. 2A**), while no significant cell composition changes were observed in non-enriched organoids (Fig. S5A).

A deeper analysis of astrocytic subpopulations by unsupervised clustering (Fig. S6 and Supplementary Table 2) revealed 11 distinct phenotypes (**Fig. 2B**) in astrocyte-enriched and 6 phenotypes in non-enriched organoids. Among the 11 phenotypes in astrocyte-enriched organoids, heartbeat sound stimulation promoted the cluster of neurotrophic and synaptogenic astrocytes (28.5 % vs 16.1 % of astrocyte cell counts, heartbeat vs control). Organoids without astrocyte enrichment showed no major changes in astrocytic subpopulations (Fig. S5B).

Heartbeat promotes synaptogenesis and activity in astrocyte-enriched organoids

Synaptogenic astrocyte differentiation revealed by scRNAseq was further supported by the upregulation of synaptic proteins detected by LC-MS/MS proteomics. Among the 137 synapse-associated proteins that were upregulated by heartbeat sound stimulation in astrocyte-enriched organoids (Fig. S7), we found multiple synaptic adhesion molecules and astrocyte-derived synapse maturation factors including Glypican 4 (GPC4).

Synaptic marker immunolabelling confirmed the increased synaptogenesis in astrocyte-enriched organoids following heartbeat sound stimulation (**Fig. 2C, C'**). Quantifications of postsynaptic puncta containing glutamate receptor subunit 1 (GLUA1), presynaptic vesicular glutamate transporter 1 (VGLUT1), and their overlaps indicated the formation of complete synapses. In cortical organoids without astrocyte enrichment, heartbeat stimulated GLUA1 clustering but not complete synapse formation (Fig. S8).

Moreover, high-density multielectrode array (HD-MEA) recordings showed significantly higher spontaneous neuronal activity in heartbeat-stimulated astrocyte-enriched organoids (**Fig. 2D, D'**). While the non-stimulated organoids exhibited little to no spontaneous electrical activity

after 31 days of maturation, in agreement with previous reports (Alam El Din et al., 2025; Trujillo et al., 2019), the heartbeat-stimulated organoids demonstrated significantly higher proportion of active units and increased mean firing rates. These results indicate that stimulation with heartbeat sound promotes functional maturation in astrocyte-enriched organoids.

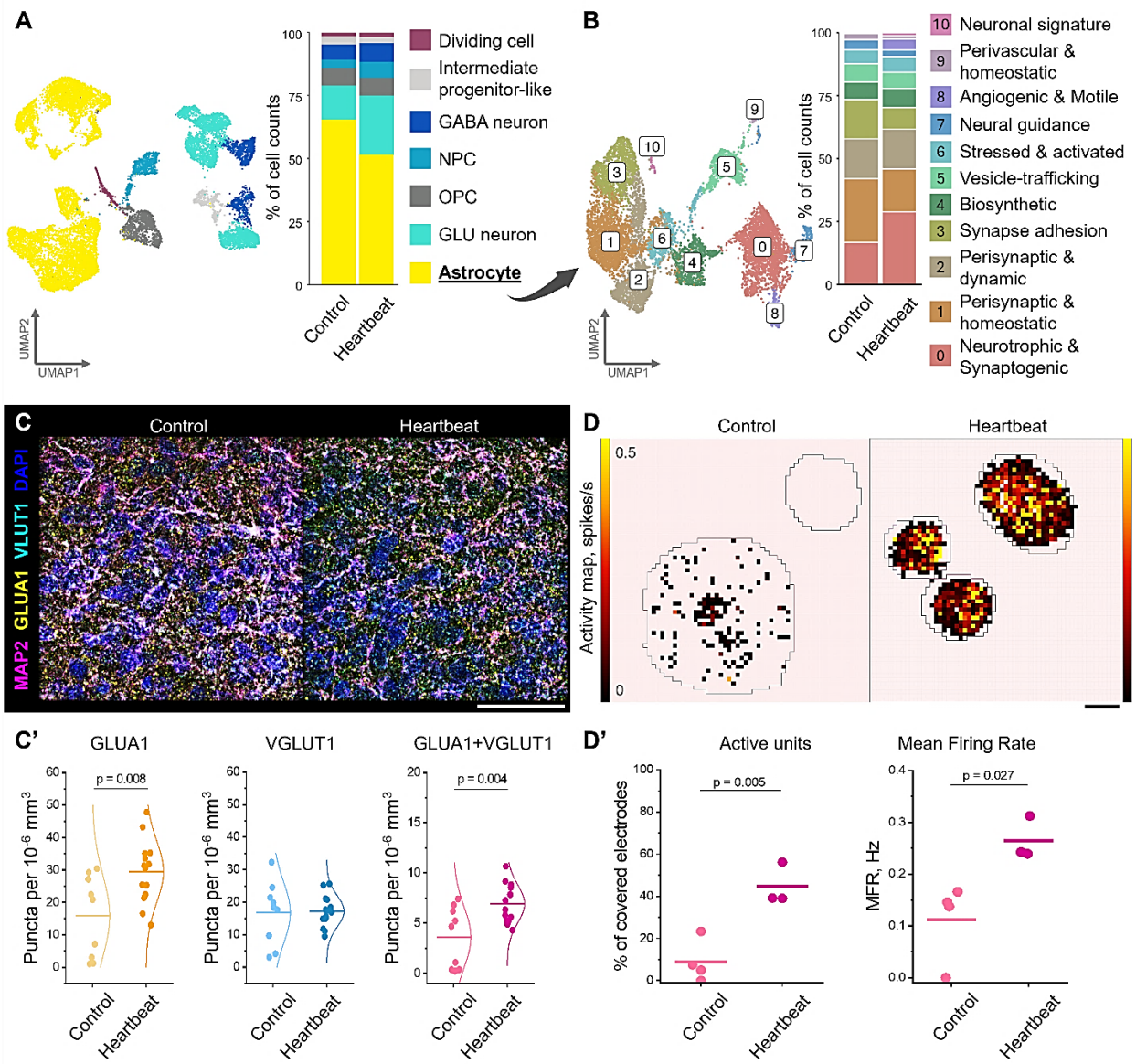

Figure 2. Stimulation with heartbeat sound promotes neural differentiation, synaptogenesis, and spontaneous activity.

(**A**) Transcriptomic UMAP map generated from scRNAseq data shows key cellular lineages in astrocyte-enriched organoids. Cell type percentages are shown as stacked bar charts. (**B**) Astrocyte subtypes revealed by cluster analysis of astrocytic transcriptomes (see Fig. S6 and Supplementary Table 2 for functional interpretation). Astrocyte subtype percentages are shown as stacked bar charts. (**C**) Immunohistochemical analysis of synaptic markers VGLUT1 (cyan) and AMPA receptor subunit GLUA1 (yellow). Neuronal dendrites are labeled with MAP2 (magenta), and nuclei (blue) are counterstained with DAPI. Scale bar, 50 µm. (**C'**) Quantifications of GLUA1, VGLUT1 synaptic puncta, and their overlaps. (n=9).

184 (**D**) Spontaneous neuronal activity in astrocyte-enriched organoids is shown by high-density multi-electrode
185 array (HD-MEA) activity maps. Scale bar, 500 µm. (**D'**) Quantifications of active units and their mean firing
186 rates (n=3-4). (**C', D'**) Statistical significance was assessed by unpaired two-tailed t-tests.

187 ***Heartbeat sound stimulates astrocytic PIEZO receptors***

188 Because sound waves propagate as mechanical deformations in a medium, we
189 hypothesized that the observed effects of heartbeat sound stimulation on organoid maturation
190 can be mediated by mechanoreceptors. scRNAseq data demonstrated that mechanosensitive
191 PIEZO1 and PIEZO2 ion channels (Coste et al., 2010) are selectively expressed by astrocytes
192 and dividing cells (**Fig. 3A**). Because dividing cells are a minor cell population (comprising < 2 %
193 of total cells), we further investigated mechanotransduction of heartbeat sound in astrocytes.

194 To perform simultaneous acoustic stimulation with heartbeat-like sound and Ca^{2+} imaging,
195 we used a custom-built device (Fig. S9), adapted from (Kumeta et al., 2025). Ca^{2+} imaging in
196 maturated iAstrocytes revealed robust responses to both short (20 s) heartbeat sound stimulation
197 (Table 1) and bath application of selective PIEZO1 agonist Yoda1 (Evans et al., 2018) (**Fig. 3B,**
198 **C**). Notably, the undifferentiated NPCs showed only minimally detectable responses to both
199 heartbeat sound and Yoda1, indicating that the heartbeat sensitivity is a feature of maturating
200 astrocytes (Fig. S10).

201 To test whether heartbeat-like sound stimulation selectively activates PIEZO1
202 mechanosensitive ion channels, we performed Ca^{2+} imaging in a human embryonic kidney
203 (HEK293) cell model lacking endogenous PIEZO1 expression (HEK293-P1KO) (Dubin et al.,
204 2017). PIEZO1 expression was induced using a plasmid vector with a fluorescent reporter
205 mScarlet to identify transfected cells (**Fig. 3D**). Both short (20 s) stimulation with heartbeat sound
206 and bath application of Yoda1 elicited sustained Ca^{2+} increase in PIEZO1-expressing cells,
207 whereas mock-transfected controls remained inactive (**Fig. 3E**). Notably, co-application of
208 heartbeat stimulation with a non-activating Yoda1 concentration (0,01 µM; IC_{50} in HEK cells ~1.3
209 µM) amplified the Ca^{2+} response, while controls remained silent, confirming the specificity of
210 PIEZO1 activation by heartbeat sound (Fig. S11).

211 ***PIEZO1 activation triggers ECM expression in mouse astrocytes***

212 To investigate the downstream effects of astrocytic PIEZO activation by low-frequency
213 sound stimulation, we applied short 1 s sound bursts with a dominant frequency of 150 Hz (Fig.
214 S12A) in primary mouse astrocytes. This mode of PIEZO1 activation evoked similar responses
215 as human heartbeat sound stimulation in HEK cells (Fig. S12B). In mouse astrocytes, short sound
216 bursts evoked more robust responses than human heartbeat sound (**Fig. 4A**, **B** and Fig. S12C-
217 F), making this PIEZO1 activation regime preferable for downstream signaling studies.

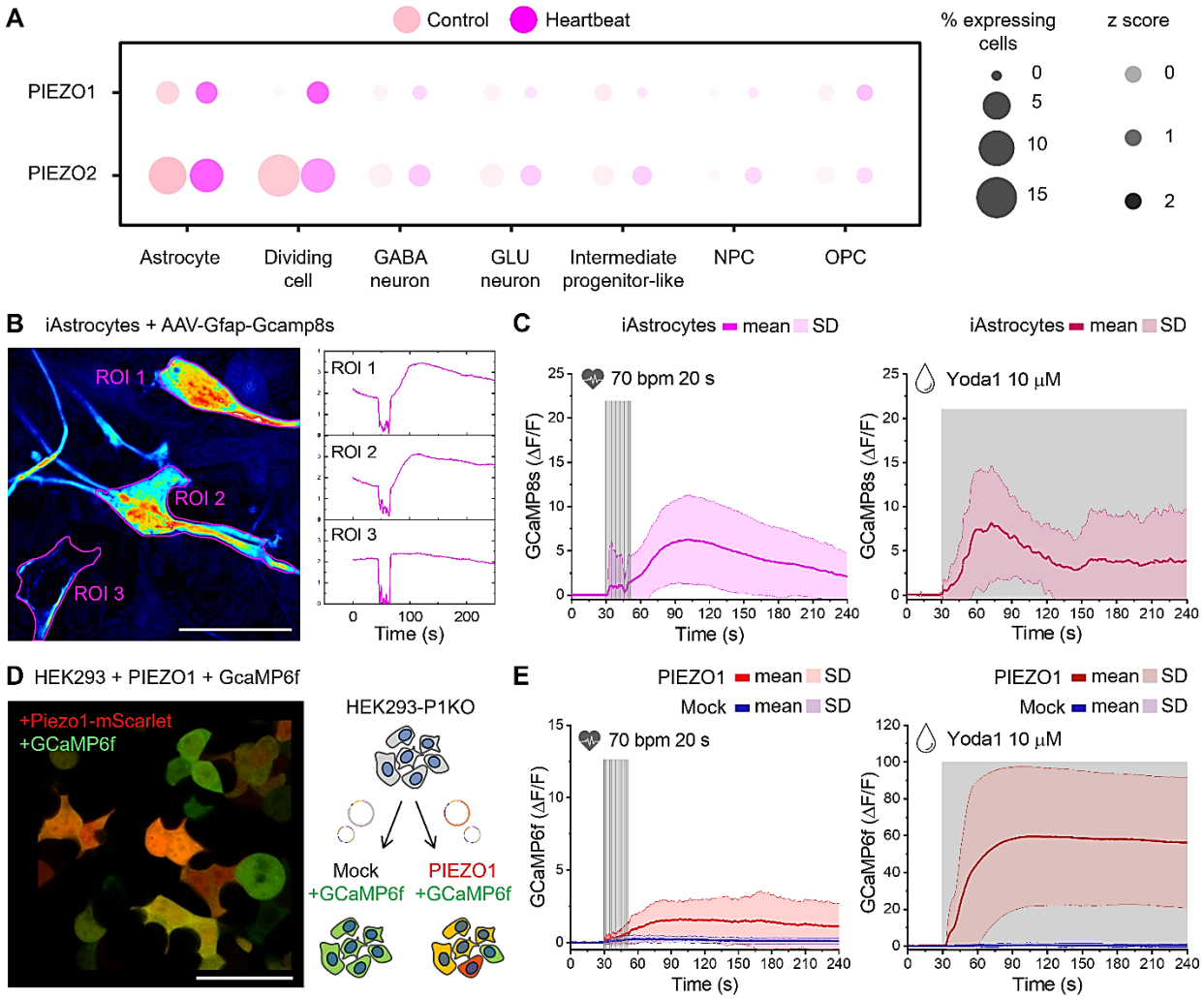

Figure 3. Astrocytic PIEZO ion channels mediate calcium responses evoked by heartbeat. (**A**) Dot plots generated from scRNAseq data show cell-specific expression of mechanosensitive PIEZO channels in astrocyte-enriched organoids. (**B**) Time-lapse t-projection and fluorescence intensity profiles show heartbeat sound-evoked Ca^{2+} responses in human iAstrocytes at 28 days of maturation. Scale bar, 50 µm. (**C**) Averaged Ca^{2+} responses evoked in iAstrocytes (magenta) by heartbeat sound stimulation and 10 µM Yoda1 application (20-25 cells, n=6). (**D** HEK293-P1KO cells were co-transfected with the GCaMP6f Ca^{2+} indicator and PIEZO1-mScarlet or Mock vectors. (**E**) Averaged Ca^{2+} responses evoked by heartbeat sound stimulation and 10 µM Yoda1 application in HEK cells with (red) and without (blue) PIEZO1 (23-39 cells, n=5). Scale bars, 50 µm.

To reveal protein expression changes induced by astrocytic PIEZO1 activation, we performed LC-MS/MS proteomics following a 3-hour incubation with 10 µM Yoda1 combined with ten acoustic bursts delivered during the first 10 minutes (**Fig. 4C**). Thereby induced astrocytic PIEZO1 activation increased the expression of ECM scaffolding components including the network-forming collagen COL8A1, pentraxin PTX3, ECM-remodeling enzymes including matrix metalloproteinases with thrombospondin motifs ADAMTS1 and ADAMTS8, and ECM-crosslinking

transglutaminase TGM1 (**Fig. 4C** and Fig. S13A). Intracellularly, PIEZO1 activation induced Ca^{2+} response and inflammation-associated transcriptional factor expression (Fig. S13B).

Biomimetic ECM hydrogels attenuate PIEZO1 activation by low-frequency sound

Because the extended activation of PIEZO1 in mouse astrocytes stimulated stress-associated pathways, we hypothesized that the brain ECM can modulate cellular responses to mechanical stimulation such as low-frequency sound. To test this hypothesis, we covered the GCaMP6f-expressing primary mouse astrocytes with ECM-mimetic hydrogels with tunable stiffness corresponding to soft and physiologically stiff brain ECM (**Fig. 4D**). Under 150 Hz sound burst stimulation, the hydrogels significantly attenuated PIEZO activation, indicated by decreased amplitude of Ca^{2+} responses and reduced fraction of responding astrocytes.

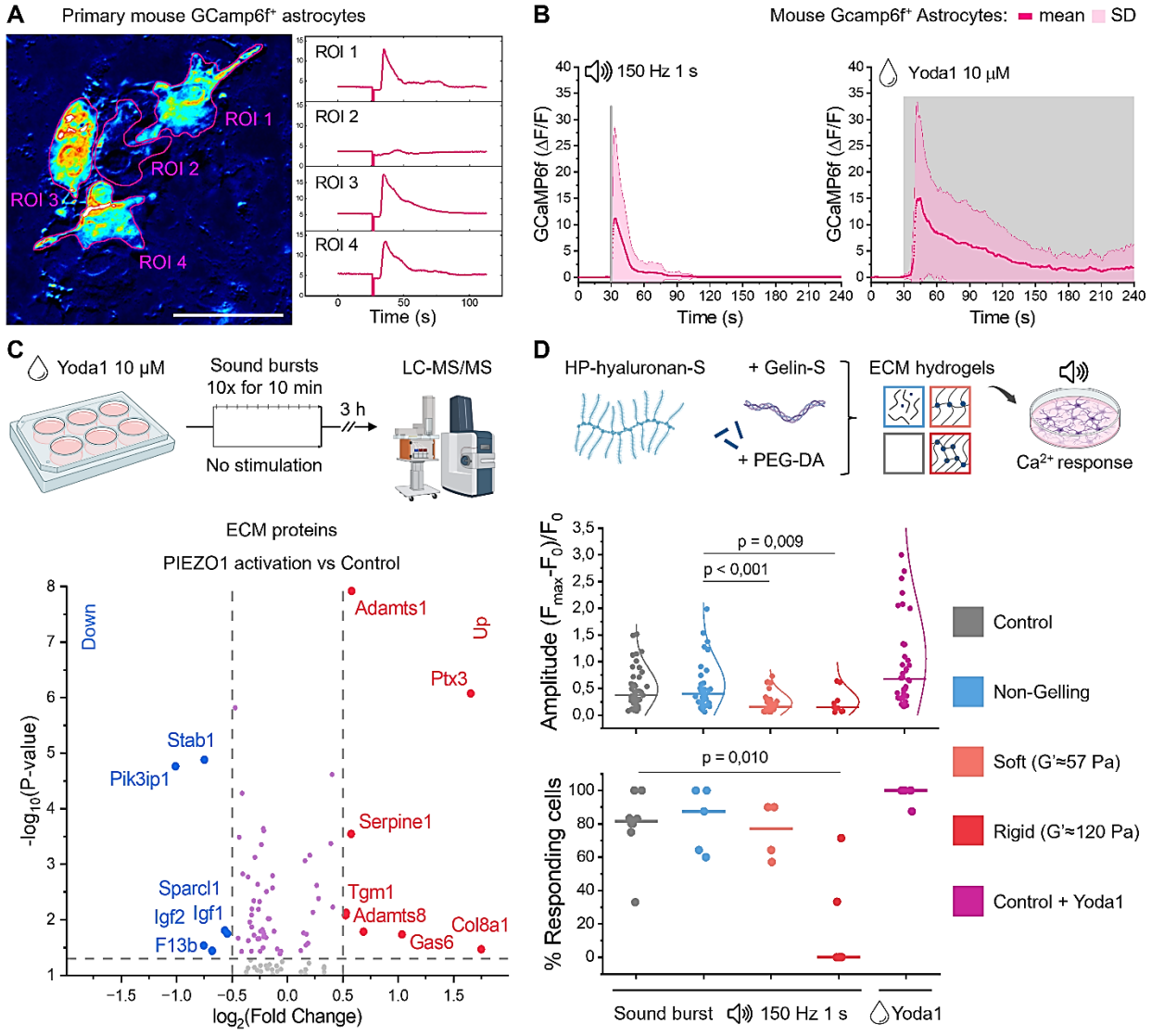

Figure 4. PIEZO1 activation and its downstream signaling in primary mouse astrocytes.

246 (**A**) Time-lapse t-projection and fluorescence intensity profiles show heartbeat-evoked Ca^{2+} responses in
247 mouse primary astrocytes. Scale bar, 50 µm. (**B**) Averaged Ca^{2+} responses evoked in astrocytes by low-
248 frequency sound bursts and 10 µM Yoda1. (38-42 cells, n=8). (**C**) LC-MS/MS measurements were
249 performed 3 hours after PIEZO1 activation in mouse astrocytes. Volcano plot shows key ECM protein
250 regulations induced by PIEZO1 activation, compared versus control. (n=5). For a full list of regulated
251 proteins see Fig. S13. (**D**) Ca^{2+} responses to low-frequency sound bursts are quantified in astrocytes
252 covered with biomimetic ECM hydrogels with variable stiffness. (n=4). Intergroup differences were analyzed
253 by one-way ANOVA followed by t-tests.

254 **DISCUSSION**

255 Our findings demonstrate a novel mechanism for activating ECM synthesis and neural
256 differentiation via mechanotransduction of physiological sound stimuli. Heartbeat sound
257 stimulation of astrocytic PIEZO ion channels promoted the differentiation of neurotrophic
258 astrocytes and glutamatergic neurons. Neural cell differentiation was accompanied by
259 coordinated expansion of ECS and ECM synthesis, which supported functional neuronal
260 maturation in human cortical organoids. This evidence suggests interoception of the internal
261 acoustic environment as an underappreciated driver of human brain development.

262 We show that the neurodevelopment and maturation promoting effects of heartbeat sound
263 stimulation in human brain organoids are astrocyte dependent. Heartbeat sound induced ECM
264 synthesis, neural differentiation, synapse formation, and spontaneous neuronal activity
265 exclusively in the astrocyte-enriched organoids. These findings align with the established role of
266 astrocytes in ECM remodeling and regulation of neuroplasticity (Dzyubenko and Hermann, 2023).
267 Consistent with the function of PIEZO ion channels in mouse hippocampal neurogenesis (Chi et
268 al., 2022), we found that activation of astrocytic PIEZO channels by heartbeat sound promoted a
269 neurotrophic and synaptogenic astrocyte phenotype. Given that our scRNAseq data
270 demonstrated predominant PIEZO expression in astrocytic lineages, these results suggest that
271 astrocytes are key interoceptors sensing and transducing internal acoustic stimuli during human
272 neurodevelopment.

273 This finding was enabled by our astrocyte enrichment protocol, which achieves a
274 physiological 1:1 astrocyte-to-neuron ratio (von Bartheld et al., 2016). Delayed astrocytic
275 differentiation and maturation in conventional human cortical organoids (Sloan et al., 2017) is a
276 limitation for investigating astrocyte-mediated mechanisms. Our approach supports the early
277 emergence of mature, ramified astrocytes. Furthermore, single-cell transcriptomics revealed
278 diverse astrocyte subtypes including perisynaptic and regulatory phenotypes, establishing this
279 model as a powerful tool for investigating astrocyte-neuronal interactions and their contributions
280 to human cortical development.

281 We demonstrate that PIEZO channels are activated by low-frequency sound stimulation
282 resembling the acoustic environment *in utero* (Gerhardt et al., 1990; Vince et al., 1982). While
283 brief 150 Hz sound bursts elicited transient PIEZO activation, rhythmic heartbeat sound with the
284 dominant frequency of 100 Hz induced sustained intracellular Ca^{2+} elevations. Continuous
285 stimulation with alternating pressure beyond 10 Hz has been shown to rapidly deactivate PIEZO1
286 (Lewis et al., 2017). However, that effect was observed during prolonged sinusoidal stimulation
287 for 4 seconds, whereas the individual heartbeat pulses used here did not exceed 0.15 seconds,
288 verified by hydrophone recordings. Consistent with previous studies showing neuronal activation
289 in response to repetitive mechanostimulation *in vitro* (Nikolaev et al., 2015) and *in vivo* (Jammal
290 Salameh et al., 2024), we demonstrate that rhythmic heartbeat sound and consecutive sound
291 bursts robustly activate mechanotransduction in astrocytes. Together with proteomic evidence for
292 upregulated Ca^{2+} responsive transcriptional factors and ECM expression, these data indicate that
293 PIEZO activation by heartbeat induces Ca^{2+}-dependent ECM synthesis in astrocytes.
294 Astrocyte-dependent ECM synthesis and ECS expansion facilitated functional maturation
295 of heartbeat-stimulated human brain organoids. While the ECS provides the diffusion routes for
296 ions and metabolites essential for neuronal activity (Sykova and Nicholson, 2008), uncontrolled
297 ECS enlargement can create “dead-space” microdomains that impair rather than facilitate
298 diffusion and signaling (Hrabetová et al., 2003). Stabilization by ECM is therefore crucial, with the
299 core scaffolding components providing a macromolecular network that binds regulatory molecules
300 (Fawcett et al., 2022), mediates neuron-glia interactions (Dzyubenko and Hermann, 2023), and
301 controls neuronal plasticity (Dityatev et al., 2010). Thus, the coordinated increase in ECM
302 synthesis and ECS volume established a homeostatic environment that supported glutamatergic
303 neuron differentiation, synapse formation, and neuronal activity following heartbeat sound
304 stimulation in astrocyte-enriched cortical organoids.
305 In addition to the maturation-associated benefits of astrocytic mechanostimulation, a
306 prolonged PIEZO activation also induced inflammatory signaling. In this context, our experiments
307 with biomimetic hydrogels indicate a mechanoprotective role of the brain ECM. By attenuating
308 PIEZO activation, physiologically stiff ECM buffers astrocytic responses to mechanical
309 stimulation. This dual role of facilitating supportive signaling while preventing excessive activation
310 suggests ECM is a homeostatic regulator of mechanotransduction in the developing brain.
311 Our findings open an intriguing direction for developing ECM-promoting therapies in
312 multiple neurological disorders that are associated with ECM degradation, including stroke
313 (Dzyubenko et al., 2023) and Alzheimer’s disease (Crapser et al., 2020). Strategies to restore
314 ECM, particularly neuron-supportive components, remain elusive. We show that these

315 components can be stimulated by low-frequency sound through astrocytic PIEZO activation.
316 While focused ultrasound has been explored for neuromodulation (Kosnoff et al., 2024), its clinical
317 translation has been limited by uncertain mechanisms. By revealing how astrocytes respond to
318 low-frequency sound, this work suggests a promising approach for harnessing astrocyte-
319 mediated ECM remodeling for neurological recovery.

320 **ACKNOWLEDGEMENTS**

321 This work was supported by the German Research Foundation (DFG, project
322 467228103 to ED; projects 504501554, 466687329 (SP4), 539301313, and 449437943
323 (A3,Z1) to DRE; projects 405358801/428817542 (within FOR2879), 449437943 (within
324 TRR332) and 514990328 to DMH). FR acknowledges funding from the Melanoma
325 Research Alliance and the Wolfgang & Gertrud Boettcher Foundation. OS acknowledges
326 funding from the ERA-NET NEURON initiative (project JTC2024 - Brain-Body: BIO-
327 PREPA). We would like to also acknowledge the Center for Advanced Imaging (CAi) at
328 Heinrich Heine University and especially Prof. Stefanie Weidtkamp-Peters and Dr.
329 Sebastian Haensch for the expert help with 3D STED imaging. For the maintenance of
330 confocal and 2P microscopes at the imaging center Essen (IMCES) facility, the authors
331 thank Dr. Anthony Squire, Dr. Jan-Hagen Krohn, and Dr. Anja Hasenberg. For support
332 with HD-MEA electrophysiology, we thank Dr. Elisa Monz (3Brain AG).

333

334 **METHODS**

335 **EXPERIMENTAL MODEL**

336 ***Human cortical organoids and induced astrocytes***

337 Neural progenitor cells (NPCs) were differentiated from a highly characterized female
338 control human induced pluripotent stem cell line (SCTi003-A). hIPSCs were plated onto low-
339 adherence AggreWell 800 plates in STEMdiff SMADi neural induction medium and 10µM of Y-
340 27632. During the next 5 days, half of the medium was replaced daily. On day 6, embryonic bodies
341 were replated on a Matrigel coated 6-well plates and full-medium changes were performed daily.
342 On day 12, neural rosette selection was performed using STEMdiff Neural Rosette Selection
343 Reagent for 1,5 hours. After re-plating, daily full-medium changes were performed until the cells
344 formed a monolayer and were ready for passaging. The resulting NPCs can be maintained further
345 with STEMdiff neural progenitor medium.

346 For quality control and as a shortcut in time-sensitive experiments, ready-to-use NPCs
347 differentiated from the same hIPSC control line (SCTi003-A) were used. Before further
348 differentiation, NPCs were expanded on Matrigel coated 6 well plates in STEMdiff neural
349 progenitor medium, during a maximum of 3 passages, using Accutase enzymatic solution for cell
350 dissociation. NPC cell bank was regularly checked upon each passage for characteristic
351 morphology and marker expression as SOX2 and Nestin, and the absence of OCT4 by
352 immunofluorescence.

353 Human induced astrocytes (iAstrocytes) were differentiated from NPCs for 3 weeks using
354 STEMdiff astrocyte differentiation medium and maturated using serum-free STEMdif astrocyte
355 maturation medium. iAstrocytes were grown on Matrigel-coated 6-well plates and passaged
356 weekly using Accutase.

357 For generating human cortical organoids, NPCs were dissociated with Accutase and
358 plated on low-adherence AggreWell 800 plates at 0.2 × 10^6 cells/well. To generate astrocyte-
359 enriched organoids, iAstrocytes at 1 week of maturation were co-seeded together with the NPCs
360 at a 2:1 ratio. Cortical organoid differentiation and maturation was achieved as described by (Birey
361 et al., 2017), with minor modifications. In brief, cortical differentiation was induced using the
362 STEMdiff dorsal forebrain organoid expansion medium containing 20 ng/ml EGF and 20 ng/ml
363 FGF2. After 14 days of differentiation, medium was replaced with the STEMdiff dorsal forebrain
364 organoid differentiation medium containing 20 ng/ml BDNF and 20 ng/ml NT3 for additional 21
365 days. During these first 35 days, medium was replaced every 2 days. For further maturation, the
366 organoids were maintained in STEMdiff neural organoid maintenance medium without

367 differentiation factors. For analysis, the organoids were transferred to imaging dishes at D45 (31
368 days of maturation).

369 ***HEK293 cells with PIEZO1 knockout (HEK293-P1KO)***

370 HEK293 cells lacking PIEZO1 (HEK293-P1KO) were maintained under standard cultivation
371 conditions in DMEM containing 25 mM glucose, 10% fetal bovine serum, and 1% penicillin-
372 streptomycin. The HEK293-P1KO cell line was kindly provided by Ardem Patapoutian's laboratory
373 (Dubin et al., 2017).

374 ***Primary mouse astrocytes***

375 Mouse astrocyte cultures were prepared from early postnatal Ai95D (Rosa-CAG-LSL-
376 GCaMP6f) mice as described previously (Borbor et al., 2023; Gottschling et al., 2016).
377 Experimental procedures were approved by the local government (Landesamt für Natur, Umwelt
378 und Verbraucherschutz, Recklinghausen) and conducted according to the European Union
379 directive 2010/63/EU and local institutional guidelines. Ai95D mice were kept in groups of 3-5
380 animals per cage with inverse 12 h light-dark cycle and *ad libitum* access to food and water.
381 Cortical mixed glial cultures were obtained from newborn (P1) male and female Ai95 mice.
382 Astrocytic monolayers were purified by cultivation in a selective medium (DMEM with 25 mM
383 glucose, 10% fetal bovine serum, and 1% penicillin-streptomycin) for 7 days. Non-astrocytic cells
384 were removed by shaking (2 hours on a rotary shaker, 150 rpm) and 20 μM cytosine-1-β-D-
385 arabinofuranoside (AraC) application for 24 hours. Purified astrocytes were sub-cultivated in the
386 defined maintenance medium (Neurobasal supplemented with 2% B27, 1 mM L-glutamine, and
387 1% penicillin-streptomycin) on glass-bottom imaging dishes (μ-Dish 35 mm #81156, Ibidi,
388 Gräfelfing, Germany) pre-coated with 1 mg/ml poly-D-lysine at 1*10^5 cells per dish density.
389 For inducing Gcamp6f expression, astrocytic monolayers were incubated with 5 μM of
390 cell-permeant nuclei-targeted TAT-Cre recombinase enzyme (#SCR508, MilliporeSigma,
391 Burlington, USA) in standard cultivation medium for 7 days before sub-cultivation on imaging
392 dishes, as described in (Dzyubenko et al., 2021).

393 **METHOD DETAILS**

394 ***Acoustic stimulation and hydrophone recordings***

395 For long-term stimulation with recorded human 70 beats per minute heartbeat (**Audio File**
396 **1**), culture dishes with organoids were maintained on top of continuously emitting (file played in a
397 loop) loudspeaker (Flatpanel CT-17803, ChiliTec) mounted inside of the cell culture incubator and
398 connected to a HiFi digital amplifier and MP3 player (Flatpanel CT-17803, sikkeby). Heartbeat

399 sound levels were adjusted to physiological sound levels (**Table 1**) using the precision
400 hydrophone (8103, HBK) measurements in cell culture medium.

401 For short-term acoustic stimulation during calcium imaging, 20 seconds of heartbeat
402 (**Audio File 1**) or 1 s sound burst (**Audio File 2**) was played using a custom-made direct
403 stimulation device (**Fig. 4B**) constructed similar to (Kumeta et al., 2025). In brief, a miniature
404 loudspeaker (8 Ohm, 1 Watt) was attached to the lid of an imaging dish used for confocal
405 microscopy. To achieve the direct transfer of acoustic waves produced by the loudspeaker, a
406 coupler (the red cap of a 15 ml falcon tube) was glued to the loudspeaker membrane. The
407 recorded sound files (**Audio File 1** or **Audio File 2**) were played via an MP3 player using the
408 trigger after the baseline calcium measurements were performed. Sound pressure levels were
409 adjusted close to maximal sound pressure levels *in utero* using the hydrophone.

410 **Table 1. Uterine sounds and acoustic stimulation of organoids**

Source	Observed during	Frequency	Equivalent 100-Hz band SPL (dB re 20 µPa)	1-Hz spectrum level (dB re 20 µPa²/Hz)	PSD (Pa²/Hz)
(Vince et al., 1982)	Gestation	100 Hz	99	79	0.029
(Querleu et al., 1988)	Gestation	223…281 Hz	92	72	0.007
(Gerhardt et al., 1990)	Gestation	0...200 Hz	110-220	90-100	0.4-4
This study	Organoid maturation with heartbeat sound	100 Hz	98	78	0.027
This study	Short stimulation with heartbeat sound during Ca^{2+} imaging	100 Hz	125	105	13.180
This study	Short sound burst stimulation during Ca^{2+} imaging	150 Hz	122	102	5.800

411 ***Calcium imaging***

412 For calcium imaging in HEK293-P1KO cell line, cells were plated on imaging dishes
413 (#81156, Ibidi) and co-transfected with 500 ng of pGP-CMV-GCaMP6f (#40755, Addgene,
414 Watertown, USA) and CMV>mPiezo1:IRES:mScarlet3 (#VB241021-1228apt, Vector Builder Inc,
415 Chicago, USA) or empty plasmid pcDNA3.1 (#138209, Addgene) as control. Transient
416 transfections were performed with lipofectamine 3000 transfection reagent (#L3000015, Thermo
417 Fisher Scientific, Oberhausen, Germany) following the manufacturer's instructions.

418 For calcium imaging in human iAstrocytes, the cells were plated on Matrigel coated
419 imaging dishes and the pAAV[Exp]-GFAP(short)>jGCaMP8s:IRES:mScarlet3:WPRE virus was
420 added at a multiplicity of infection (MOI) of 5*10^4 for 3 hours. Calcium imaging was performed 1
421 week after transduction.
422 For calcium imaging in NPCs, the cells were plated on Matrigel coated imaging dishes
423 and cultivated until monolayer. Thirty minutes before the scans, the culture medium was replaced
424 with Neurobasal medium supplemented with 2% SM1 neuronal supplement and Fluo-4 AM at a
425 final concentration of 5 µM for 30 minutes. Calcium responses were recorded for 5-6 minutes per
426 region of interest including 1 minute baseline at 37°C using the Leica TCS SP8 confocal
427 microscope with a 20x objective. Single plane 129.42x129.42 µm images (pixel size 253x253 nm)
428 were acquired at 0.188 seconds per frame rate). Calcium spikes were detected as (Fmax-
429 Fmin)/Fmin, using standard imageJ selection and measurement tools and custom-written Matlab
430 scripts (**Supplementary Code 1**).

431 ***Superresolution 3D STED (SuSHi) and 2P shadow imaging***

432 For visualizing the extracellular environment in living organoids, we adapted the SuSHi
433 technique from (Tonnesen et al., 2018). For stability, the organoids were attached to glass-bottom
434 imaging dishes coated with 1:30 diluted Matrigel for 5-10 hours prior to imaging experiment.
435 3D STED microscopy was performed from the bottom of the organoid, starting 5 µm above
436 the attachment site to avoid potential artifacts from Matrigel coating. For 3D STED shadow
437 imaging, organoid culture medium was supplemented with 200 µM non-cell permeable calcein.
438 3D STED microscopy was performed using a Leica 3D gSTED SP8 microscope (93x glycerol
439 immersion objective with motor correction, HC PL APO 93x/1,30 GLYC motCORR STED WHITE,
440 and 75% 3D STED). Motor correction was adjusted for maximum resolution at 10 µm imaging
441 depth. Z-stacks (125x125x15 µm, voxel size 61x61x150 nm) were obtained between 5 and 20
442 µm from the coverslip. Apparent resolution was estimated by measuring the full width at half-
443 maximum (FWHM) of the smallest visible structures at 10 µm depth (**Supplementary Table 1**).
444 2P microscopy was performed from the top of the organoid, and resolution at 100 µm
445 depth was estimated by FWHM of the smallest detectable structures (**Supplementary Table 1**).
446 For 2P shadow imaging, organoid culture medium was supplemented with 200 µM non-cell
447 permeable Lucifer Yellow. 2P microscopy was performed using a Leica TCS SP8 (25x HCX
448 IRAPO L 25x water immersion objective, NA 0.95) microscope. ROIs (295.3x295.3x115 µm, voxel
449 size 85x85x699 nm) were scanned as z-stacks. The excitation laser (Titanium:Sapphire
450 Chameleon Vision II) was tuned to 890 nm, and the 15% of 1.7 W output power was used. Emitted
451 fluorescence (500 - 570 nm detection wavelength) was collected using a hybrid detector.

452 ***Immunolabeling procedures***

453 For immunocytochemistry, samples were fixed with 4% PFA for 10 min (2D cell cultures)
454 or 30 min (organoids) at room temperature (RT). Permeabilization and pre-blocking was applied
455 for 2 hours at RT (2D cells) and 5 hours (organoids) with PBS pH 7.0 containing 0.15% Triton X-
456 100 (2D cells) or 0.3% Triton X-100 (organoids), 10% Chemiblocker and 2% donkey serum.
457 Primary antibodies were applied overnight at 4˚C , and secondary antibodies conjugated to
458 fluorescent dyes were used for detection. Nuclei were counterstained with DAPI.

459 To enable 3D confocal imaging of large organoid volumes, optical index of tissues was
460 matched to the target objective immersion by sequential incubation in 50% and 97% 2,2′-
461 thiodiethanol (TDE) for 20 minutes, followed by mounting in 97% TDE on imaging dishes.

462 ***Microscopy and immunofluorescence quantifications***

463 Image stacks for marker protein quantification in organoids were acquired using the Leica
464 3D gSTED SP8 microscope with a 20x Plan-Apochromat objective, numerical aperture (NA) 0.8.
465 ROIs (472.3x472.3x5.5 µm, 124x124x500 nm) were scanned as Z-stacks and converted to
466 maximum intensity projections. Image analysis was performed using standard tools in ImageJ.

467 High-resolution images for synapse quantification in organoids were acquired using the
468 confocal microscope LSM710 (Carl Zeiss) with a 63x Plan-Apochromat objective (NA 1.4). Three
469 random ROIs (90x90x5.5 µm, voxel size 88x88x457 nm) per organoid were scanned Z-stacks.
470 3D synapse quantification was performed using the Synapse counter plugin for ImageJ
471 (Dzyubenko et al., 2016)

472 ***High-density multielectrode (HD-MEA) electrophysiology***

473 Spontaneous activity was recorded using the BioCAM DupleX paired with CorePlate 1W
474 38/60 MEA plates (3Brain AG). Organoids were plated onto the electrode field, and immobilized
475 for recording with the 3D printed meshes (3Brain GmbH, Lanquart, Switzerland). Before
476 recordings, organoids were equilibrated for 1 hour in the incubator. Network activity was recorded
477 for 5 minutes at 37°C using Brainwave 5 software. The recordings were acquired at 20 kHz
478 sampling rate.

479 ***Biomimetic ECM hydrogels***

480 Biomimetic hydrogels with adjustable stiffness were produced using the HyStem-HP
481 Hydrogel Kit (Advanced Biomatrix) according to manufacturer's instructions. Gel stiffness was
482 tuned to 0, 57, and 120 Pa shear storage moduli by adjusting the concentration of crosslinking
483 reagent (PEGDA). Before polymerization, gel components were pre-mixed with the cultivation

484 medium and applied in 250 µl droplets onto astrocytic monolayers. After 2 hours, the gels were
485 completely polymerized, and Ca^{2+} imaging was performed 24 hours later.

486 ***LC-MS-MS proteomics***

487 Human cortical organoids or mouse primary astrocytes were washed in cold PBS and
488 lysed in 30 µl of lysis buffer (Tris-HCl, 150 mM NaCl, 1% SDS, pH 7.8) supplemented with
489 complete mini EDTA free protease inhibitor. Samples were treated with 2,5 U Benzonase and
490 sonicated in a water bath twice for 5 minutes each, and centrifuged at 5000 g for 10 min to remove
491 cell debris. Protein concentration was determined using a BCA assay.

492 Tryptic digestion was performed for 16 hours at 37° C using the single-pot, solid-phase-
493 enhanced sample preparation (SP3) protocol (Hughes et al., 2019) with trypsin-to-protein ratio of
494 1:30. Eluted peptides were dried in an Eppendorf Concentrator Plus (Eppendorf SE, Hamburg,
495 Germany) and stored at minus 80° C until further use. Directly prior to measurement, peptides
496 were reconstituted in 20 µl of 0.1% FA and centrifuged at 16,000 g for 5 minutes to remove
497 remaining beads. The peptide concentration was estimated using a NanoDrop Microvolume
498 Spectrometer (Thermo Fischer Scientific, Waltham, USA) at 205nm.

499 For human cortical organoids, 50 ng of peptides were loaded onto an Evotip (Evosep
500 Biosystems, Odense, Denmark) following the manufacturer instructions. Peptide separation was
501 performed on an Evosep One (Evosep Biosystems, Odense, Denmark) using the predefined
502 Wisper Zoom 40 SPD method on an Aurora Elite CSI size C18 UHPLC column (15 cm length, 75
503 um inner diameter, 1.7 µm particle size, 120 Å pore size (IonOpticks, Collingwood, Australia)).

504 For primary mouse astrocytes, 200 ng of peptides were injected into a Nanoelute2 LC
505 system (Bruker Daltronics, Brillerica, Massachusetts, USA). Peptides were loaded onto a PepMap
506 Neo Trap Cartridge (5 mm length, 300 um inner diameter, 5 um particle size, 100 Å pore size;
507 Thermo Fisher Scientific, Massachusetts, USA) and analyzed using a 50-min chromatography
508 gradient on an Aurora Ultimate CSI 18 capillary column (25 cm length, 75 um inner diameter, 1.7
509 um particle size, 120 Å pore size (IonOpticks, Collingwood, Australia) consisting of mobile phase,
510 A (0.1% FA in H20) and mobile phase B (0.1% FA in ACN-H2O), ranging from 2-34% B at a flow
511 rate of 300nL/min.

512 Eluting peptides were injected into an TimsTOF HT mass spectrometer (Bruker Daltronics,
513 Brillerica, Massachusetts, USA), via a CaptiveSpray source at 1600V. The mass spectrometer
514 was operated in data-independent acquisition (DIA) PASEF mode. The accumulation and ramp
515 time for the dual TIMS analyzer were set to 100ms at a ramp rate of 9,42 Hz. Scan ranges were
516 set to m/z 100-1700 for the mass range and 1/k0 0.60-1.60Vs-1cm-2 for the mobility range at both
517 MS levels. For DIA-PASEF, a cycle time of 1.8 seconds was estimated. Within each cycle, a

518 precursor mass range of 400 to 1201 Da and a mobility range of 0.6 to 1.6 1/K0 was fragmented.
519 At MS1 level, one ramp was executed per cycle. For MS/MS measurements 32 MS/MS windows
520 with a mass width of 26.0 Da each and a mass overlap of 1.0 were distributed across the 16
521 MS/MS ramps.

522 ***Single-cell RNA sequencing***

523 Single-cell suspensions were obtained by digesting 20 organoids per condition in 1 ml of
524 lysis buffer containing 30U of papain, 13mM of L-cysteine, and 125 U of DNAse1. The lysis buffer
525 was pre-activated for 20 minutes at 37°C, and the organoids were dissociated using a rotary
526 shaker at 500 rpm and 37°C for 45 min and by pipetting up and down every 5 minutes.
527 In each sample, between 12.000 and 20.000 cells were loaded onto a GEM-X single-cell
528 3' chip. Sequencing-library construction was performed by following the GEM-X 3' assay v4 (10x
529 Genomics) protocol. Sequencing was performed using the Novaseq X plus (Illumina) platform
530 aiming for 30k reads per cell (PE150).

531 **QUANTIFICATION AND STATISTICAL ANALYSIS**

532 ***ECS volume***

533 Segmentation of cellular and extracellular organoid compartments for ECS volume quantifications
534 in 3D STED and 2P shadow imaging was performed using trainable Weka segmentation in
535 ImageJ. Raw images were preprocessed, non-organoid masks detected by custom plugin and
536 subtracted from the segmented extracellular space (Fig. S2 and **Supplementary Code 2**).

537 ***Spontaneous activity***

538 For spike detection, the high-pass filter (100 Hz) was applied, and the sliding window
539 differential threshold algorithm implemented in Brainwave 5 software. A threshold of 9*SD of the
540 noise was used, sliding window length 2ms, and the timestamps were assigned to the negative
541 peak of the action potentials. For spike sorting we used the Legendre moments algorithm for
542 feature extraction paired with a K-means & Silhouette algorithm for clustering. Mean firing
543 frequency of each active unit was calculated for the entire recording time. Only units with a mean
544 firing frequency higher than 0.05 Hz were considered. Bursts were defined as series of 5
545 consecutive spikes occurring within a 100ms window.

546 ***LC-MS-MS data quantifications***

547 LC-MS raw data were processed using the direct DIA algorithm in Spectronaut (Version
548 19.1.240806.626, Biognosys, Schlieren, Switzerland), applying BSG factory settings (Enzyme/
549 Cleavage rules: Trypsin/P; Fixed modification: Carbamidomethyl (C); Variable modifications:
550 Acetyl (Protein N-term) and Oxidation(M)), against a reviewed human UniProt/Swissprot FASTA
551 database (from 13th of March 2024, containing 20418 target sequences) for human cortical
552 organoids and against a reviewed murine UniProt/Swissprot FASTA database (from 13th of
553 March 2024, containing 17196 target sequences). Quantification was performed at the MS2 level.
554 Imputation was disabled. Cross run normalization was enabled. Normalized protein abundance
555 was used for further downstream analysis, exported and analyzed in R.

556 Protein abundances were log2 transformed to approach the Gaussian probability
557 distribution. Differentially abundant proteins between multiple predefined phenotypes were
558 determined by analysis of variation (ANOVA). Significantly regulated proteins ($p<0.05$) were
559 subjected to further analysis. Differentially abundant proteins between pairs of predefined
560 phenotypes were determined by Student's t-testing. Proteins showing significant differences
561 ($p<0.05$, fold change > 1.5) were subjected to further analysis. Heatmaps were generated based
562 on hierarchical clustering results. The Pearson correlation was used as a distance metric at the
563 sample and protein level respectively. Ward.D2 linkage was applied. Prior to heatmap generation,
564 log2 protein abundances were centered around the mean per protein for visual purposes. For
565 principal component analysis, a missing data-tolerant nonlinear PCA (NIPALs-PCA) was used.

566 ***Single-cell RNA sequencing quantifications***

567 Raw sequencing data was processed using CellRanger (version 9.0.1) and aligned to the
568 human reference genome (GRCh38). Initial quality control was performed to retain cells with more
569 than 1000 and less than 8000 detected genes, and less than 10% mitochondrial reads. Doublets
570 were identified and removed using DoubletFinder (rate=8%). After quality filtering, a total of
571 44,743 cells remained for downstream analysis.

572 Data integration and clustering were performed using the Seurat package (Hao et al.,
573 2024) in R. The filtered data was processed using NormalizeData, FindVariableFeatures, and
574 ScaleData functions. Dimensionality reduction was first performed using RunPCA. Batch effects
575 between different experimental conditions were then corrected using Harmony (Korsunsky et al.,
576 2019) integration based on the PCA results. Visualization was achieved using RunUMAP, and
577 unsupervised clustering was performed using FindNeighbors and FindClusters based on the
578 Harmony embeddings with dims = 1:20 and resolution = 0.3. Cortical organoid single-cell spaces

were manually cured by removing fibroblasts. All violin plots, heatmaps, and feature plots were drawn using standard plotting functions from R, Seurat, and SeuratExtend package (Hua et al., 2025). Astrocyte signature intensities were measured using the Bioconductor package AUCell (Aibar et al., 2017).

Statistical analysis of imaging and electrophysiology data

Data were analyzed in OriginPro2025 (OriginLab, Northampton, MA, U.S.A.). The normality of data distributions was verified by Shapiro-Wilk mothod. Differences between group means were analyzed using one or two -way mixed model ANOVA with Tukey's multiple comparisons adjustment, followed by pairwise posthoc comparisons using t-tests. In all experiments, the significance level was set as $\alpha=0.05$, and the $p<0.05$ values indicated significant differences between groups.

591 **Table 2. Key resources.**

REAGENT or RESOURCE	SOURCE	IDENTIFIER
Antibodies		
Sheep polyclonal anti-Neurocan	R&D Systems	Cat# AF6508
Mouse monoclonal anti-GLUA1 (extracellular)	Synaptic Systems	Cat# 182 011
Rabbit polyclonal anti-Vglut1	Synaptic Systems	Cat# 135 303
Guinea Pig polyclonal anti-MAP2	Synaptic Systems	Cat# 188 004
Rat monoclonal anti-GFAP (clone 2.2B10)	ThermoFisher	Cat# 13-0300
Rabbit polyclonal anti-SOX2	Abcam	Cat# ab97959
Mouse monoclonal anti-Nestin (clone 110C2)	StemCell Technologies	Cat# 60091AD
Mouse monoclonal anti-OCT4 (clone 3A2A20)	StemCell Technologies	Cat# 60093AD
STARRED FluoTag-X4 anti-Rabbit IgG	NanoTag	Cat# N2404
Alexa647 anti-Sheep IgG (H+L)	Jackson Immuno	Cat# 713-605-003
Alexa488 anti-Mouse IgG (H+L)	Life Technologies	Cat# A21202
Alexa594 anti-Rat IgG (H+L)	Life Technologies	Cat# A21209
Alexa647 anti-Genea Pig IgG (H+L)	Jackson Immuno	Cat# 706-605-148
Bacterial and virus strains		
pAAV[Exp]-GFAP(short)> jGCaMP8s:IRES:mScarlet3:WPRE	VectorBuilder	#AAVdjM(VB241018-1367mxv)-K1
Chemicals, peptides, and recombinant proteins		
hESC-grade Matrigel	Corning	Cat# 354277
mTeSR Plus medium	StemCell Technologies	Cat# 100-0276
STEMdiff SMADi neural induction medium	StemCell Technologies	Cat# 08581
Y-27632	StemCell Technologies	Cat# 72302
STEMdiff Neural Rosette Selection Reagent	StemCell Technologies	Cat# 05832
STEMdiff Neural Progenitor Medium	StemCell Technologies	Cat# 05833
STEMdif Astrocyte Differentiation Kit	StemCell Technologies	Cat# 100-0013
STEMdiff Astrocyte Serum-Free Maturation Kit	StemCell Technologies	Cat# 100-1666
STEMdif Dorsal Forebrain Organoid Differentiation Kit	StemCell Technologies	Cat# 08620
STEMdiff Neural Organoid Maintenance Kit	StemCell Technologies	Cat# 100-0120
Accutase	StemCell Technologies	Cat# 07920
cytosine-1-β-D-arabinofuranoside (AraC)	Sigma-Aldrich	Cat# C6645
DMEM	Gibco	Cat# 11966
B27	Gibco	Cat# 17504-001
poly-D-lysine	Sigma-Aldrich	Cat# A-003-E
TAT-Cre recombinase	Sigma-Aldrich	Cat# SCR508
Papain	Sigma-Aldrich	Cat# P3125
L-cysteine	Sigma-Aldrich	Cat# 5501

DNAse 1	Roche	Cat# 11284932001
Protease inhibitors	Roche	Cat# 11836170001
Lipofectamine 3000	ThermoFisher	Cat# L3000015
Neurobasal medium	Life Technologies	Cat# A2477501
SM1 supplement	StemCell Technologies	Cat# 05711
Fluo-3	ThermoFisher	Cat# F1241
Calcein	Biotium	Cat# 80013
Lucifer Yellow	Sigma-Aldrich	Cat# L0259
DAPI	Sigma-Aldrich	Cat# D9542
Chemiblocker	Millipore	Cat# 2170
2,2′-thiodiethanol	Sigma-Aldrich	Cat# 166782
HyStem-HP Hydrogel Kit	Advanced Biomatrix	Cat# GS315F
Fetal bovine serum	Gibco	Cat# A5256701
Penicillin-streptomycin	Gibco	Cat# 15070-063
L-glutamine	PAN Biotech	Cat# P04-80050
Triton X-100	Calbiochem	Cat# 648462
Donkey serum	Sigma-Aldrich	Cat# D9663
Sodium chloride	Carl Roth	Cat# 9265.2
ROTI Stock 20 % SDS	Carl Roth,	Cat# 1057.1
Complete mini-EDTA free tablets	Roche	Cat# 11836170001
Benzonase Nuclease	Sigma-Aldrich	Cat# E1014-5KU
1.4- Dithiothreitol (DTT)	Roche	Cat# 10708984001
Iodoacetamide (IAA)	Sigma Aldrich	Cat# I1149-5G
Tris ultrapure	Applichem	Cat# A1086
Ammonium Bicarbonate (ABC)	Sigma Aldrich	Cat# 09830-500G
Calcium chloride solution, CaCl2	Sigma Aldrich	Cat# 21115-250ML
Sequencing grade Modified Trypsin	Promega	Cat# V5111
Dimethyl sulfoxide (DMSO)	Sigma Aldrich	Cat# D5879-100ML
Formic Acid 99+%	Thermo Scientific	Cat# 289905
Acetonitril (ACN), LC-MS Grade	Thermo Scientific	Cat# 51101
2-Propanol ROTISOLV ≥99,95 %, LC-MS Grade	Carl Roth	Cat# AE73.2
Water for LC-MS	Applichem	Cat# 701074.1611
Evotip Pure, Tips	Evosep	Cat# EV2013
Ethanol ROTISOLV ≥99,95 %, LC-MS Grade	Carl Roth	Cat# 1HP8.1
Sera-Mag Magnetic Carboxylate	Cytiva	Cat# 44152105050250
Sera-Mag Magnetic Carboxylate	Cytiva	Cat# 24152105050250
Critical commercial assays		
BCA assay	ThermoFisher	Cat# 23225
Deposited data		
Raw and analyzed proteomic data	This paper, PRIDE database	Project accession: PXD069523 Token: w8rfTmHC1Kqx
Raw and analyzed transcriptomic data	GEO database	
Raw and analyzed	Dryad database	Dryad token

Experimental models: Cell lines		
Healthy Control Human iPSC Line, Female, SCTi003-A	StemCell Technologies	Cat# 200-0511
Human iPSC-Derived Neural Progenitor Cells	StemCell Technologies	Cat# 200-0620
HEK293-P1KO	Ardem Patapoutian's lab	(Dubin et al., 2017)
Experimental models: Organisms/strains		
Rosa-CAG-LSL-GCaMP6f (Ai95D) mice	The Jackson Laboratory	Strain #028865
Oligonucleotides		
Recombinant DNA		
CMV>mPiezo1:IRES:mScarlet3	VectorBuilder	#VB241021-1228apt
pGP-CMV-GCaMP6f	Addgene	#40755
pcDNA3.1	Addgene	#138209
Software and algorithms		
R software environment version 4.1.2	The Comprehensive R Archive Network (CRAN)	https://ftp.fau.de/cran/
Seurat package (version 5.3.0)	(Hao et al., 2024)	https://cran.r-project.org/web/packages/Seurat/index.html
SeuratExtend (version1.2.3)	(Hua et al., 2025)	https://github.com/huayc09/SeuratExtend
Harmony (version 1.2.3)	(Korsunsky et al., 2019)	https://cran.r-project.org/web/packages/harmony/index.html
Bioconductor package AUCell	(Aibar et al., 2017)	https://bioconductor.org/packages/release/bioc/html/AUCell.html
OriginPro 2025 version (64-bit) SR1	OriginLab Corporation	https://www.originlab.com/
ImageJ	(Schneider et al., 2012)	https://imagej.nih.gov/ij/
Catman (version 5.6.3)	HBK	https://www.hbkworld.com/en/products/software/daq/catman-data-acquisition-software
Other		
AggreWell 800 24-well plates	Stem Cell Technologies	Cat# 34850
Glass Bottom Dish 35 mm	Ibidi	Cat# 81218-200
Hydrophone	Hottinger Brüel & Kjær	Cat# 8103

AK-45 Digital Audio Amplifier	sikkeby	https://www.amazon.de/HiFi-Verst%C3%A4rker-Stereo-Audioverst%C3%A4rker-Endverst%C3%A4rker-Soundverst%C3%A4rker-USB-Karteneingang/dp/B0BXD288TM?th=1
Flatpanel CT-17803 loudspeaker	ChiliTec	https://www.amazon.de/products_id-78311-Flatpanel-Lautsprecher-40W-schwarz/dp/B00BVZX1KE/ref=ast_sto_dp_puis
MP3 Sound-Chip Module	WayinTop	https://www.amazon.de/WayinTop-Beschreibbares-Programmierbare-Herunterladbar-Aufladbarer/dp/B07X7G7DZG/ref=ast_sto_dp_puis
Supplementary audio file 1	This paper	n/a
Supplementary audio file 2	This paper	n/a
Supplementary Video 1	This paper	n/a
Supplementary Video 2	This paper	n/a
Supplementary Video 3	This paper	n/a
Supplementary Video 4	This paper	n/a
Supplementary Video 5	This paper	n/a
Supplementary Video 6	This paper	n/a
Supplementary Video 7	This paper	n/a
Supplementary Video 8	This paper	n/a

SUPPLEMENTARY FILES AND CODE

Supplementary Videos 1-8

Supplementary Codes 1-3

Supplementary audio files 1-2

Supplementary figures and tables

Supplementary Table 1. Shadow imaging resolution.

	3D STED	2P
	10 µm depth	100 µm depth
n	FWHM, nm	FWHM, nm
1	150	540
2	130	460
3	210	320
4	130	400
5	140	590
6	150	440
7	120	310
8	130	
9	150	
10	120	
11	200	
12	180	
13	210	

601 **Supplementary Table 2. Astrocyte clusters and their function.**

	Cluster name	Upregulated genes	Rationale
Astrocyte-enriched organoids			
0	Neurotrophic & Synaptogenic	MDK, IGFBP2, RSPO3, FBLN1, CDH7, TSPAN7, NELL1, ITM2C/BRI2, CLYBL, SPARCL1, WNT7B	Astrocytes enriched for trophic and axon-guidance factors (MDK, IGFBP2, NELL1), Wnt potentiation (RSPO3), ECM assembly (FBLN1), adhesion (CDH7) and EV-linked synapse modulators (TSPAN7), consistent with astrocyte-driven synapse maturation and astro support. These cells likely enhance neurite growth and synaptogenesis while stabilizing the perisynaptic microenvironment.
1	Perisynaptic & Homeostatic	GJA1, DBI, SCD, TXNIP, MT2A, CPE, PMP2, S100B, EDNRB, AHCYL1, ID2, GABBR2, PCDH9, BCAN	Defined by canonical astrocyte markers (S100B, GJA1, DBI, MT2A, TXNIP) plus BCAN, PCDH9, and GABBR2, this state is related to synapse regulation and homeostatic astrocyte responses to Ca^{2+} oscillations
2	Perisynaptic & Dynamic	DBI, TXNIP, BCAN, AHCYL1, TFPI, WLS, CREB1L, ARID5B, FSTL5, SNCAIP, EDNRB, ID2	Characterized by Wnt secretion (WLS), synapse interaction adhesion molecules (FSTL5, SNCAIP), and CREB-mediated transcriptional reprogramming, this state combines homeostatic ECM support (BCAN, DBI, TFPI) with enhanced potential for synaptic remodeling and plasticity
3	Synapse adhesion	PCDH9, ADGRB3, TNIK, GREB1L, PPP2R2B, LRRC4C, MIR99AHG, GLIS3, CTNND2, SNCAIP, FSTL5, NEAT1	Enrichment of synapse adhesion regulators together with NEAT1, defines a perisynaptic, adhesion-rich astrocyte state that stabilizes and modulates synaptic contacts; reduced ribosomal/EIF1/RACK1 and vimentin indicates a mature, low-biosynthesis, non-reactive profile
4	Biosynthetic	PMP2, MT2A, SCD, DBI, S100B, RACK1, FTH1, RPLP1, RPLP0, RPL15, RPS28, RPL13A, RPL13 RPS14, RPS8, RPL41	Marked by ribosomal gene enrichment and reduced developmental adhesion programs (NFIA, ZBTB20, NPAS3, RORA; LSAMP, ADGRV1), this state reflects a translation-high phenotype

5	Vesicle-trafficking & Synaptogenic	CD9, CDH7, S100A10, S100A6, TSPAN7, NELL2, CAV1, ETNPPL, ANXA2, YBX3, VIM, SPARCL1	Enrichment of tetraspanins and vesicle-associated genes defines an astrocytic phenotype specialized for exosome- and caveolae-mediated membrane trafficking and intercellular signalling
6	Stressed & Activated	RACK1, UCHL1, SQSTM1, CEBPB, CCPG1, SARS, DDIT3, TCEA1, HSPA9, EIF1	This phenotype combines adaptive responses to stress with reduced protein synthesis and upregulated hypoxia-activated genes
7	Neural patterning & guidance	ZBTB20, EIF4G3, LSAMP, PHACTR1, NFIA, ADGRV1, NPAS3, LRP1B, RORA, NELL1, GLIS3, KALRN	Enrichment of transcriptional factors associated with differentiation, morphogenesis, and adhesion indicates a patterning and contact-guidance astrocytic phenotype
8	Angiogenic & motile	PTN, NR2F2-AS1, PDE1A, EEF1A1, H3F3A, WNT7B, NR2F2, C1orf61, FABP7, RND3, MARCKSL1	This cluster combines neurovascular signature (WNT7B, NR2F2, PTN) with a radial glia like expression (FABP7, RND3, MARCKSL1) and Ca^{2+} signaling, indicating these astrocytes can migrate and promote vascular development.
9	Perivascular & homeostatic	S100A6, KCTD1, LHFPL6, NKX2-1, MGP, ATP1A2, EMP2, CALD1, CYSTM1, APOE	This phenotype shows genes related to astrocytic end feet at blood-brain barrier interfaces (ATP1A2, APOE, EMP2, CALD1), secreted matricellular cues (SPARCL1, CD9, S100A10, ANXA2), and ventral telencephalon identity (NKX2-1)
10	Neuronal signature	GRIA2, DLGAP1, NRXN1, ANK3, MYT1L, KALRN, NAV3	Canonical neuronal gene expression associated with neurite and synapse development, possibly indicating phagocytic astrocytes contributing to synaptophagy and therefore incorporating neuronal mRNA

Cortical organoids without astrocyte enrichment			
0	Neurotrophic & Synaptogenic	ETNPPL, PLP1, RSPO3, WNT7B, PHACTR1, RMST, NR2F2-AS1, SPARCL1, ADGRV1, ADAMTSL1, FBLN1, NRXN3, CSRP2, NELL2, AC092957.1	Astrocytes strongly expressing neurotrophic and synaptogenesis regulators (RSPO3/WNT7B) together with synapse-promoting (SPACRL1) and ECM/adhesion organizers (NRXN3, ADGRV1, ADAMTSL1, FBLN1), consistent with astrocytes that produce trophic cues and actively promote excitatory synaptogenesis.
1	Homeostatic & Secretory	PTGDS, MT3, C1orf61, CPE, B2M, ID2, CLU, PI15, PCDH9, PPP2R2B	Homeostatic astrocytes enriched with secreted chaperones and neuroprotective signals (CLU, CPE, PTGDS, MT3), while expressing synapse-associated molecules (PCDH9/PPP2R2B) to stabilize and tune astrocyte-neuronal interactions
2	Synaptogenic & ECM-remodeling	CST3, SPARCL1, S100A10, ADAMTSL1, CD9, TNC, LGALS1, FBLN1, CSRP2, NELL2	These astrocytes promote and stabilize excitatory synapses (SPARCL1, CSRP2) exporting extracellular vesicles (CD9), and sculpting perisynaptic matrix (CST3, ADAMTSL1, TNC, FBLN1/ADAMTSL1)
3	Stress-adaptive	FTL, FTH1, CDKN1A, EIF1, RACK1, TKT, RPS27L, RPL19, RPS13, GAS5	Astrocytes with upregulated DNA repair (CDKN1A, RPS27L), antioxidant response (GAS5, TKT, RACK1, EIF1) and ferroptosis-regulating genes (FTH1, FTL).
4	Hypoxia-adaptive	IGFBP2, IGFBP5, BNIP3, VEGFA, PGK1, TRIM2, SLC2A1, FAM162A, HILPDA, P4HA1	These astrocytes show the hypoxia-associated metabolic switch pattern (GLUT1, PGK1, VEGFA), cellular remodeling (BNIP3, HILPDA, P4HA1), and trophic control (IGFBP2/5) in hypoxic niches.
5	Neuronal signature	ANK3, NAV3, SNHG14, GRIA2, CELF4, FAM155A, FGF14, NLGN1, PPFIA2, DLG2	This cluster is enriched with canonical neuronal transcripts found in axons (ANK3, NAV3) and synapses (FGF14, GRIA2, DLG2, NLGN1, PPFIA2), possibly indicating synaptophagic astrocytes

602

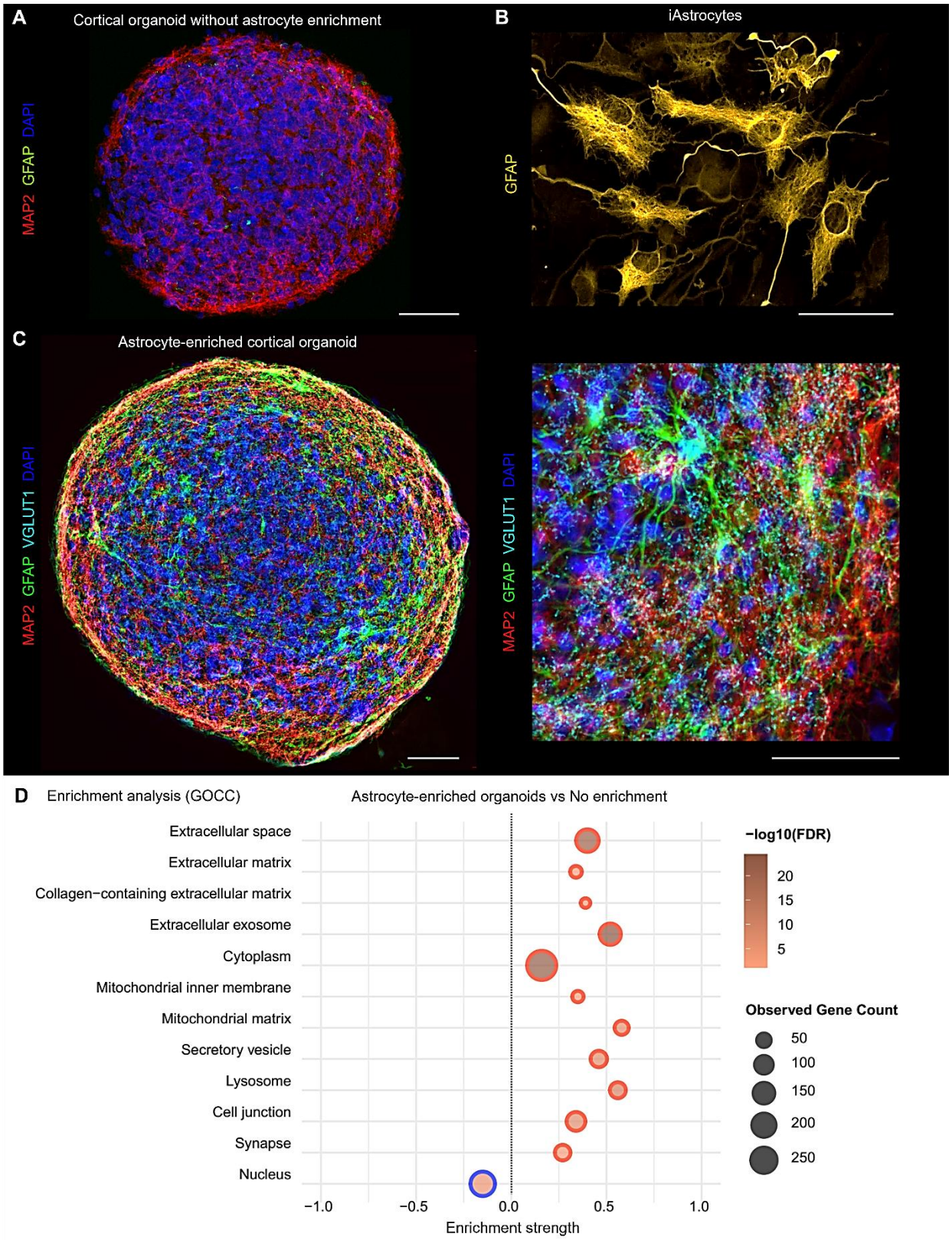

Supplementary Figure 1. Generation of astrocyte-enriched human cortical organoids.

605 (**A**) Without astrocyte enrichment, cortical organoids at day 45 contained few astrocytes (GFAP, green).
606 (**B**) For astrocyte enrichment, pre-differentiated human induced astrocytes (iAstrocytes, GFAP, yellow)
607 were co-cultured with neural precursor cells (NPCs) during organoid formation. (**C**) Astrocyte-enriched
608 organoids develop networks of ramified astocytes (GFAP, green), mature neurons (MAP2, red), and
609 establish glutamatergic synapses (VGLUT1m cyan) at 45 days of cultivation. (**D**) Gene ontology cellular
610 component analysis (GOCC) based on significantly regulated proteins ($p < 0.05$, fold change difference >
611 1.5, t-test) measured with LC-MS/MS. The analysis shows upregulated extracellular matrix, secretory
612 programs, and synaptic proteins in astrocyte-enriched vs non-enriched organoids (n=6). Scale bars, 50 µm.
613

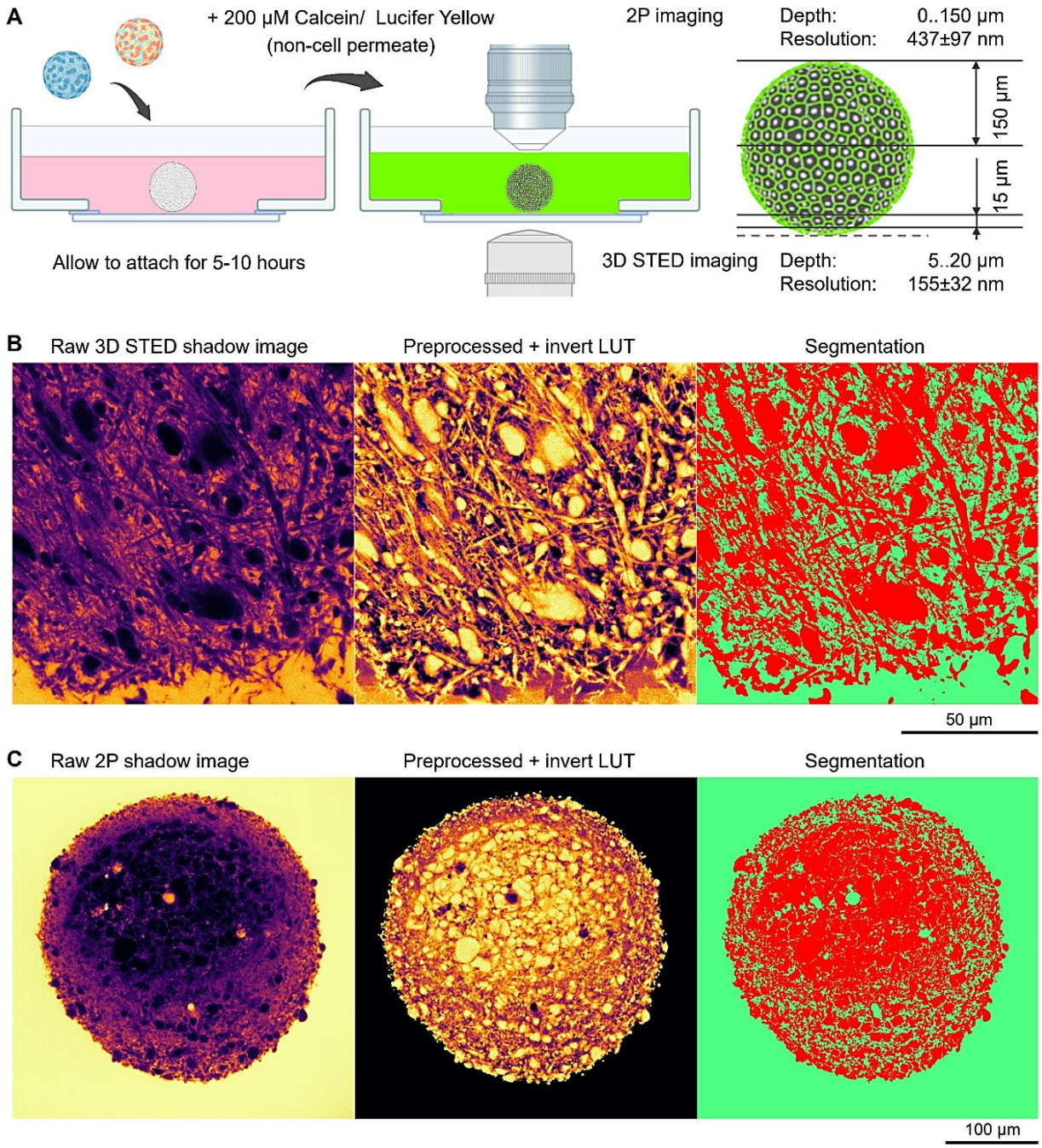

Supplementary Figure 2. Shadow imaging and image processing.

(**A**) Strategy for visualizing the organoid extracellular space (ECS). Organoids were attached to glass-bottom imaging dishes coated with 1:30 diluted Matrigel for stability. 3D STED microscopy was performed from the bottom of the organoid, starting 5 µm above the attachment site to avoid potential artifacts from Matrigel coating. Apparent resolution at 10 µm depth was estimated by measuring the full width at half-maximum (FWHM) of the smallest visible structures. 2P microscopy was performed from the top of the organoid, and resolution at 100 µm depth was estimated by FWHM of the smallest detectable structures. (**B, C**) Segmentation of cellular (red) and extracellular (green) organoid compartments for ECS volume quantifications in 3D STED and 2P shadow imaging.

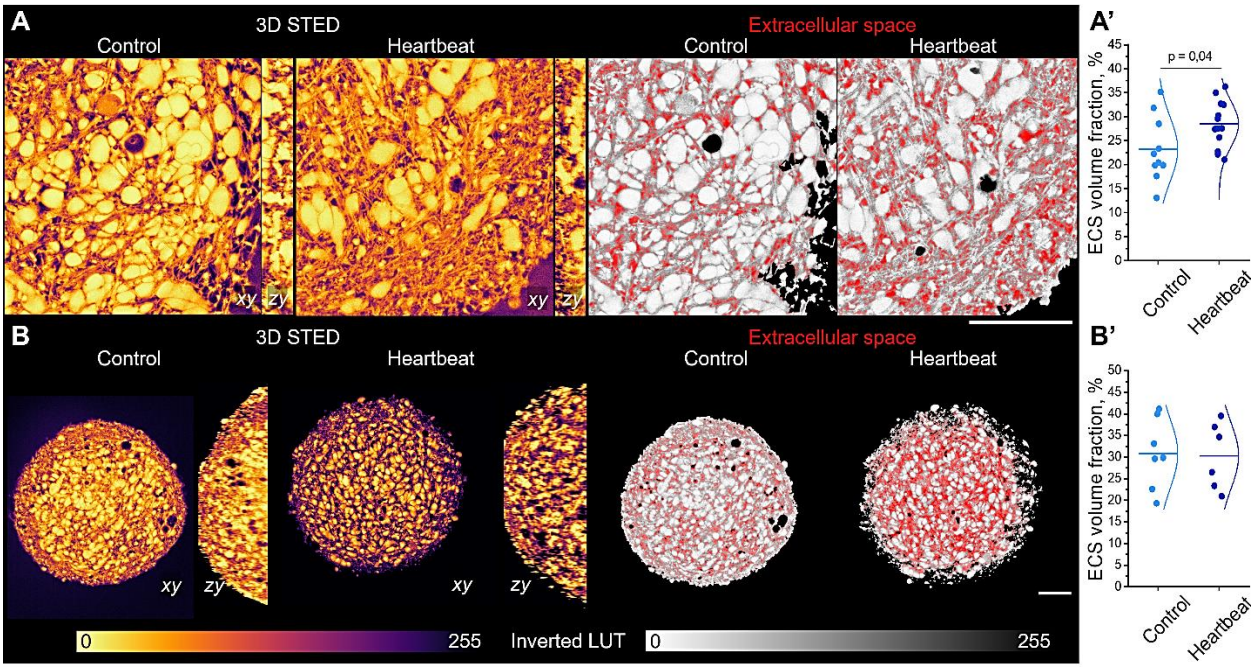

Supplementary Figure 3. Shadow imaging and ECS volume in human cortical organoids without astrocyte enrichment.

(**A**) Superresolution 3D STED shadow imaging and ECS segmentation (red) in live organoids. (**A'**) ECS volume fraction comparison, t-test (n=10-15). (**B**) 2P shadow imaging and ECS segmentation (red) in live organoids. (**B'**) ECS volume fraction comparison, t-test (n=5-6). (**C**, **D**) Images are xy and zy projections; LUT inverted. Scale bars, 50 µm.

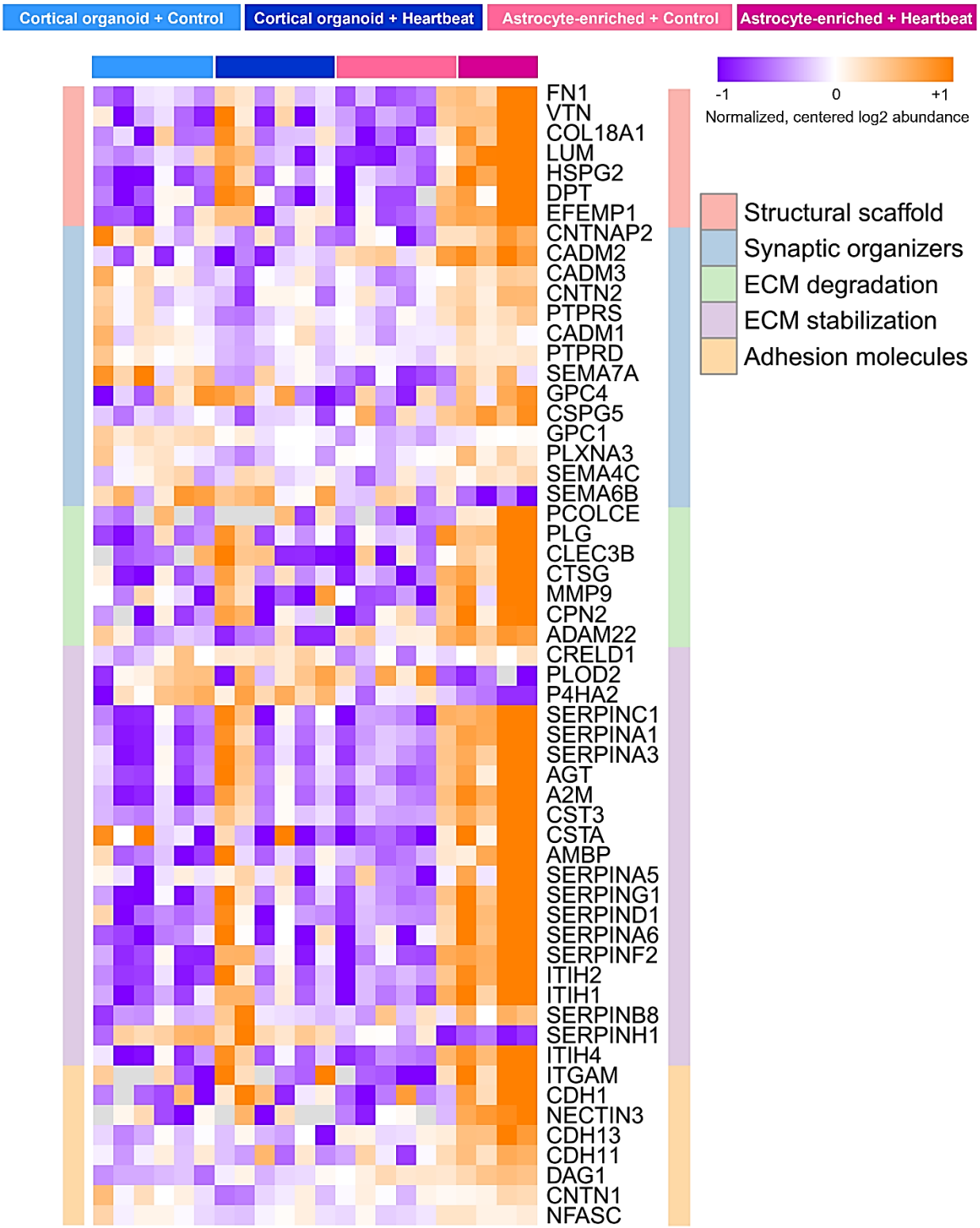

Supplementary Figure 4. ECM proteins regulated by heartbeat.

Heatmap shows normalized, centered log2 protein abundances for ECM proteins found significantly different ($p<0.05$, t-test) between astrocyte-enriched+control versus astrocyte-enriched+heartbeat groups.

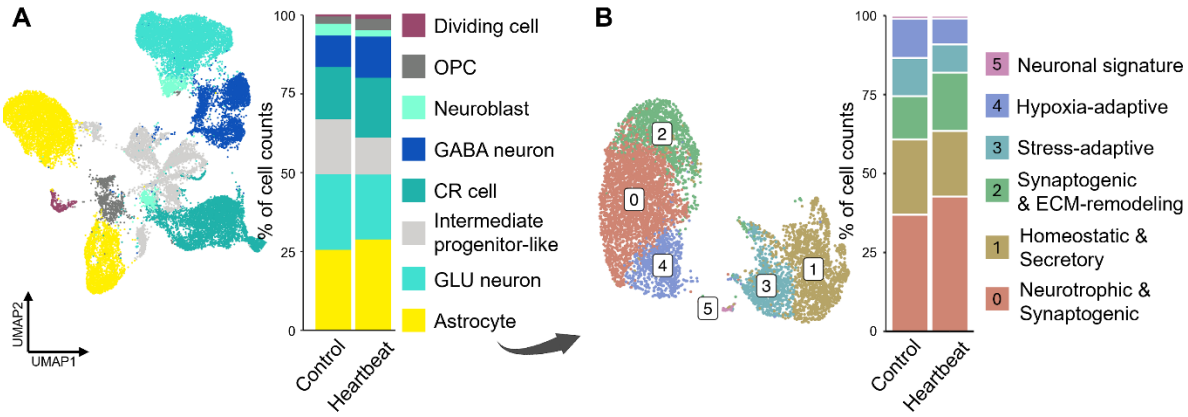

Supplementary Figure 5. Cellular composition of cortical organoids without astrocyte enrichment. (**A**) Transcriptomic UMAP map generated from scRNAseq data shows key cellular lineages. (**B**) Astrocyte subtypes revealed by cluster analysis of astrocytic transcriptomes (see Fig. S6 and Supplementary Table 2 for functional interpretation).

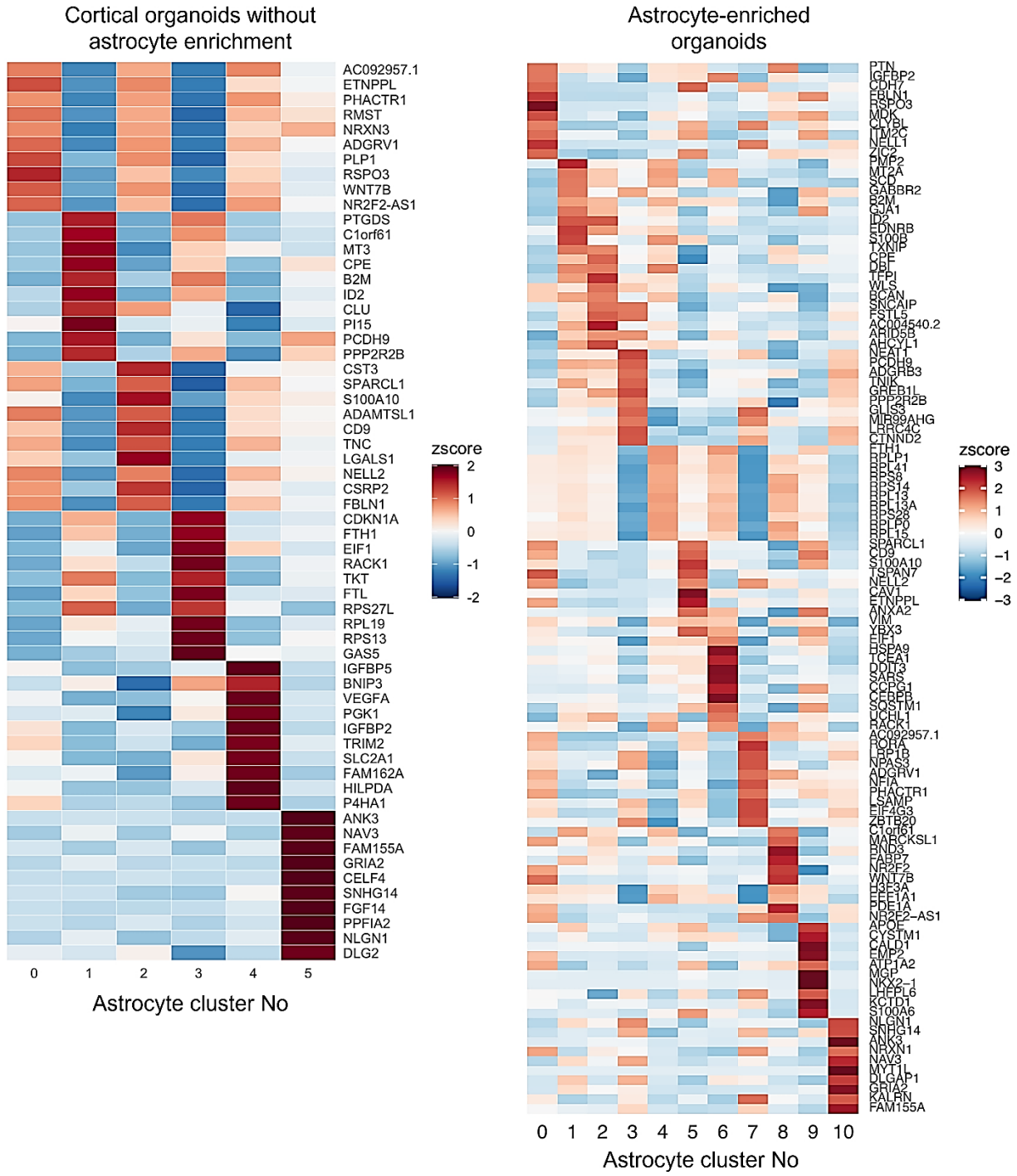

Supplementary Figure 6. Astrocytic subpopulations identified by scRNA sequencing.

Heatmaps show z-scores of key genes differentially expressed in astrocytic subpopulations identified by unsupervised cluster analysis. For functional interpretation, see **Supplementary Table 2**.

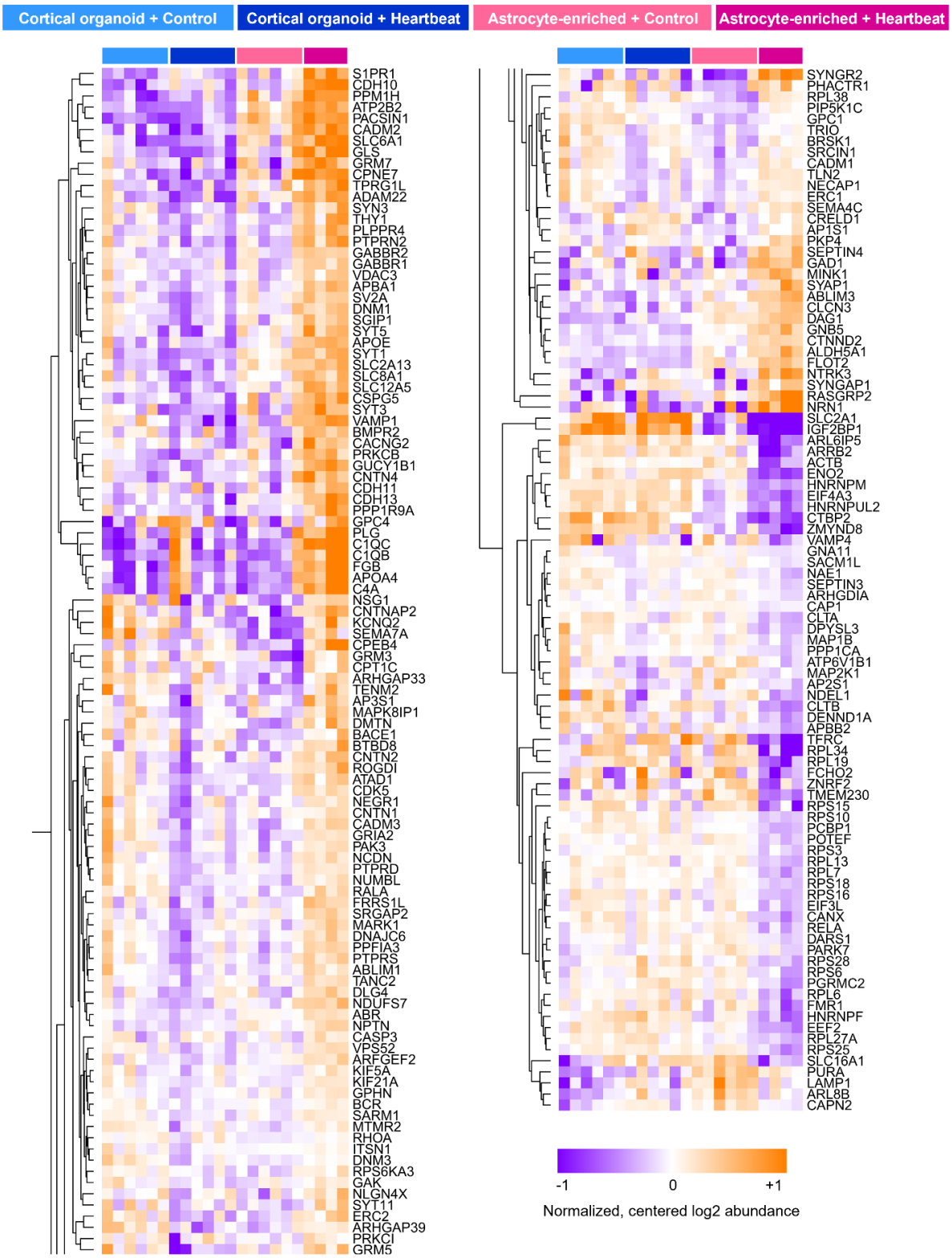

Supplementary Figure 7. Synapse-associated proteins regulated by heartbeat. Heatmap shows normalized, centered log2 protein abundances for synapse-regulating proteins found significantly different ($p<0.05$, t-test) between astrocyte-enriched + control versus astrocyte-enriched + heartbeat groups.

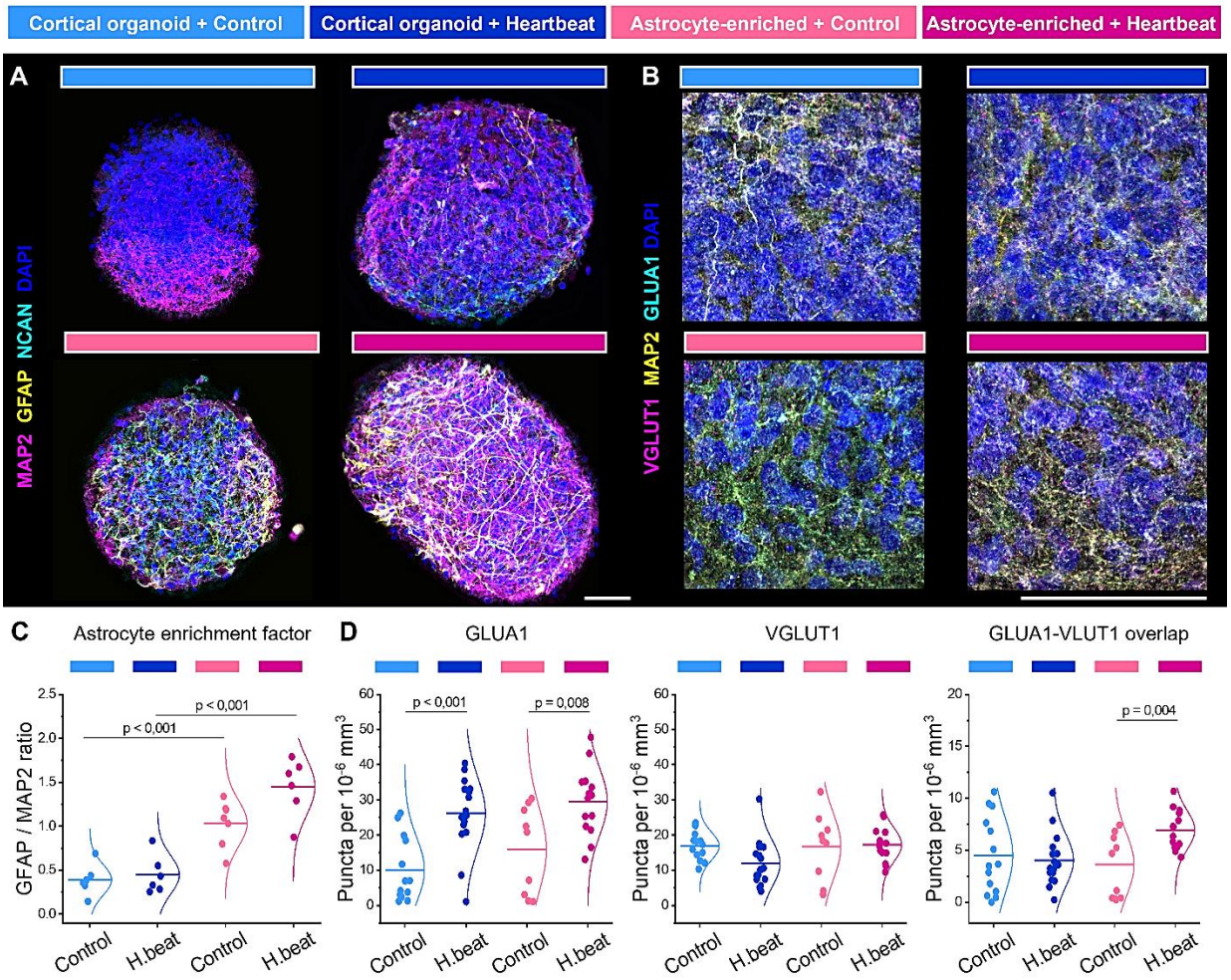

Supplementary Figure 8. Synaptogenesis in astrocyte-enriched and non-enriched organoids. (**A**) Immunolabeling of neurons (MAP2, magenta), astrocytes (GFAP, yellow), and neurocan (NCAN, cyan) indicates the enrichment of ramified astrocytes, quantified in (**C**) as the GFAP/MAP2 fluorescence intensity ratio (n=6). (**B**) Immunohistochemical analysis of synaptic markers VGLUT1 (magenta) and AMPA receptor subunit GLUA1 (cyan). Neuronal dendrites are labeled with MAP2 (yellow). (**A, B**) Nuclei (blue) are counterstained with DAPI. Scale bars, 50 µm. (**D**) Quantifications of GLUA1, VGLUT1 synaptic puncta, and their overlaps. (n=9). (**C, D**) Intergroup differences were analyzed by two-way ANOVA followed by t-tests.

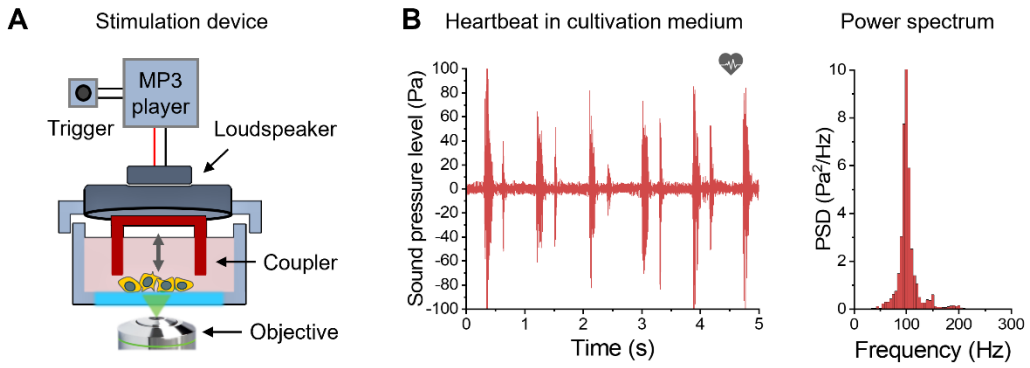

Supplementary Figure 9. Direct acoustic stimulation in the medium. (A) Custom-made device for direct acoustic stimulation in the medium. A miniature loudspeaker (8 Ohm, 1 Watt) was attached to the lid of an Ibidi dish used for confocal imaging. To achieve the direct transfer of acoustic waves produced by the loudspeaker, a circular coupler was glued to the loudspeaker membrane. The recorded heartbeat was played via an MP3 player with a trigger. (B) Hydrophone recording and power spectrum of the applied heartbeat stimulation.

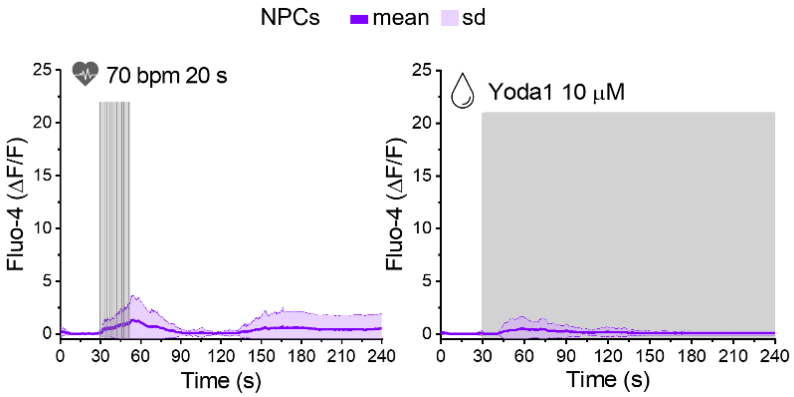

Supplementary Figure 10. Ca^{2+} responses to heartbeat sound stimulation in NPCs. Averaged Ca^{2+} responses evoked by heartbeat and 10 µM Yoda1 application in NPCs were measured using the Fluo-4 Ca^{2+} indicator. (14-20 cells, n=5)

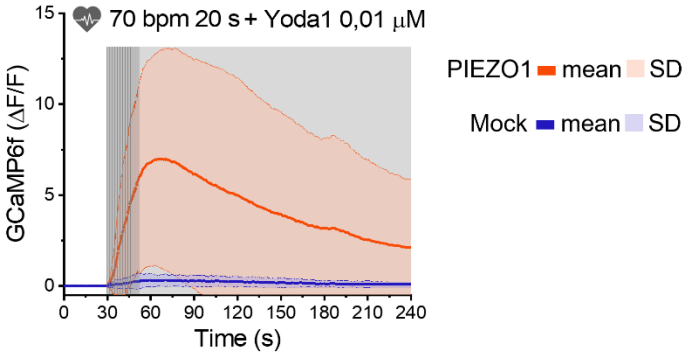

Supplementary Figure 11. Ca^{2+} responses to heartbeat sound stimulation in HEK293 cells. Averaged Ca^{2+} responses evoked by co-application of 0.01 µM Yoda1 and heartbeat sound stimulation (47 cells, n=7)

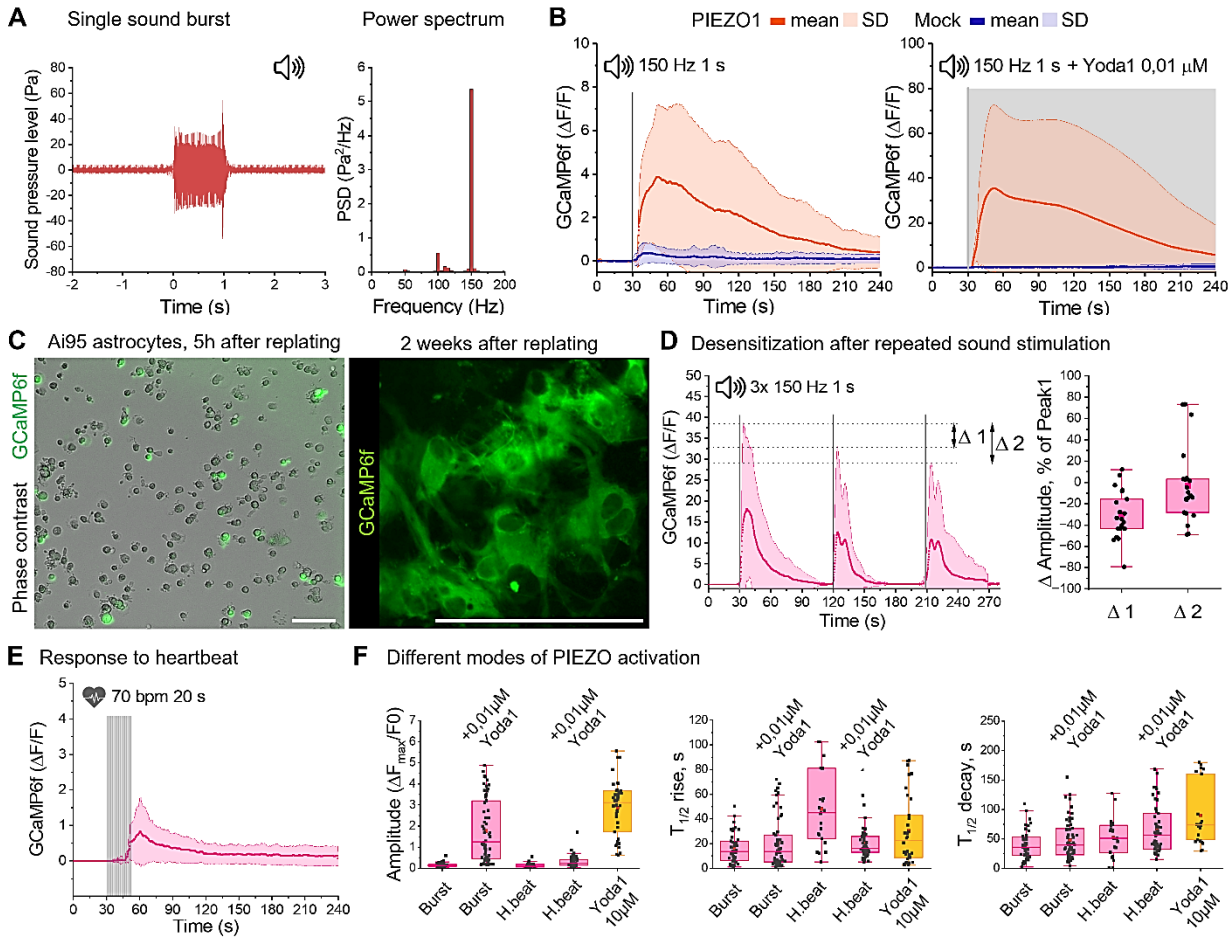

Supplementary Figure 12. Ca^{2+} responses to low-frequency sound stimulation in primary mouse astrocytes.

(**A**) Hydrophone recording and power spectrum of short 150 Hz frequency sound burst stimulation. (**B**) Averaged Ca^{2+} responses to short (1 s) sound bursts in HEK293-P1KO cells co-transfected with PIEZO1-mScarlet (orange) or Mock control (blue) and GCaMP6f. Co-application of a non-activating 0.01 μM Yoda1 concentration and sound bursts amplified PIEZO-mediated Ca^{2+} responses (49-62 cells, n=7). (**C**) Primary astrocyte cultures were prepared from Ai95 (Rosa-CAG-LSL-GCaMP6f) mice, and GCaMP6f expression was induced by TAT-iCre recombinase. One week later, astrocytes were replated onto glass-bottom imaging dishes, and Ca^{2+} imaging was performed in monolayers 2 weeks after replating. Scale bars, 100 μm. (**D**) Ca^{2+} responses to three consecutive 1 s sound bursts delivered at 90-s intervals showed reduced amplitudes compared to the first response, indicating desensitization (21 cells, n=10). (**E**) Averaged Ca^{2+} responses to heartbeat stimulation in primary astrocytes (41 cells, n=12). (**D**) Comparison of different modes of PIEZO1 activation in astrocytes: a single 150-Hz sound burst with (62 cells, n=7) or without (43 cells, n=7) 0.01 μM Yoda1, heartbeat-like stimulation with (54 cells, n=8) or without (23 cells, n=4) 0.01 μM Yoda1, and 10 μM Yoda1 without acoustic stimulation (39 cells, n=5).

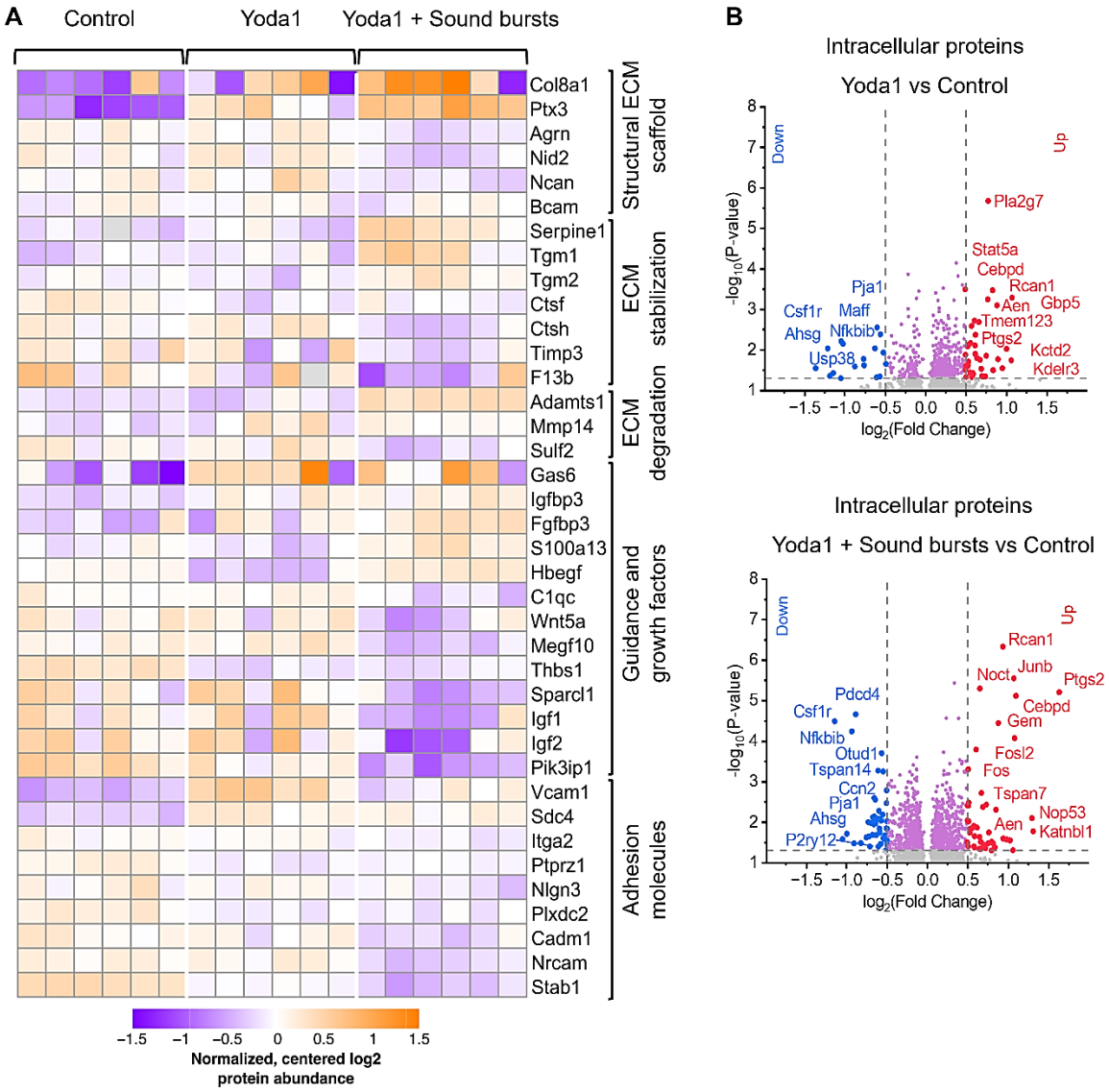

Supplementary Figure 13. Protein expression changes induced by PIEZO1 activation in primary mouse astrocytes.

(**A**) Heatmap shows normalized, centered log2 protein abundances for ECM proteins found significantly different ($p<0.05$, t-test) between Yoda1 + sound burst stimulation versus Yoda1 stimulation versus control astrocyte cultures, measured by LC-MS/MS. (**B**) Volcano plots show major regulations of intracellular proteins induced in mouse astrocytes by Yoda1 + sound burst stimulation and Yoda1 stimulation versus control, detected my LC-MS/MS.

References

Aibar, S., González-Blas, C.B., Moerman, T., Huynh-Thu, V.A., Imrichova, H., Hulselmans, G., Rambow, F., Marine, J.C., Geurts, P., Aerts, J., *et al.* (2017). SCENIC: single-cell regulatory network inference and clustering. Nat Methods *14*, 1083-1086.

Alam El Din, D.-M., Moenkemoeller, L., Loeffler, A., Habibollahi, F., Schenkman, J., Mitra, A., van der Molen, T., Ding, L., Laird, J., Schenke, M., *et al.* (2025). Human neural organoid microphysiological systems show the building blocks necessary for basic learning and memory. Communications Biology *8*, 1237.

Birey, F., Andersen, J., Makinson, C.D., Islam, S., Wei, W., Huber, N., Fan, H.C., Metzler, K.R.C., Panagiotakos, G., Thom, N., *et al.* (2017). Assembly of functionally integrated human forebrain spheroids. Nature *545*, 54-59.

Borbor, M., Yin, D., Brockmeier, U., Wang, C., Doeckel, M., Pillath-Eilers, M., Kaltwasser, B., Hermann, D.M., and Dzyubenko, E. (2023). Neurotoxicity of ischemic astrocytes involves STAT3-mediated metabolic switching and depends on glycogen usage. Glia *71*, 1553-1569.

Chi, S., Cui, Y., Wang, H., Jiang, J., Zhang, T., Sun, S., Zhou, Z., Zhong, Y., and Xiao, B. (2022). Astrocytic Piezo1-mediated mechanotransduction determines adult neurogenesis and cognitive functions. Neuron *110*, 2984-2999.e2988.

Coste, B., Mathur, J., Schmidt, M., Earley, T.J., Ranade, S., Petrus, M.J., Dubin, A.E., and Patapoutian, A. (2010). Piezo1 and Piezo2 are essential components of distinct mechanically activated cation channels. Science *330*, 55-60.

Crapser, J.D., Spangenberg, E.E., Barahona, R.A., Arreola, M.A., Hohsfield, L.A., and Green, K.N. (2020). Microglia facilitate loss of perineuronal nets in the Alzheimer's disease brain. EBioMedicine *58*, 102919.

Dealessandri, G., and Vivalda, M. (2018). The mother’s womb acoustic environment: study of the original sounds and replication for pre-term infants. Journal of Physics: Conference Series *1075*, 012056.

Dityatev, A., Schachner, M., and Sonderegger, P. (2010). The dual role of the extracellular matrix in synaptic plasticity and homeostasis. Nat Rev Neurosci *11*, 735-746.

Dubin, A.E., Murthy, S., Lewis, A.H., Brosse, L., Cahalan, S.M., Grandl, J., Coste, B., and Patapoutian, A. (2017). Endogenous Piezo1 Can Confound Mechanically Activated Channel Identification and Characterization. Neuron *94*, 266-270.e263.

Dzyubenko, E., and Hermann, D.M. (2023). Role of glia and extracellular matrix in controlling neuroplasticity in the central nervous system. Semin Immunopathol *45*, 377-387.

Dzyubenko, E., Prazuch, W., Pillath-Eilers, M., Polanska, J., and Hermann, D.M. (2021). Analysing Intercellular Communication in Astrocytic Networks Using "Astral". Front Cell Neurosci *15*, 689268.

Dzyubenko, E., Rozenberg, A., Hermann, D.M., and Faissner, A. (2016). Colocalization of synapse marker proteins evaluated by STED-microscopy reveals patterns of neuronal synapse distribution in vitro. J Neurosci Methods *273*, 149-159.

Dzyubenko, E., Willig, K.I., Yin, D., Sardari, M., Tokmak, E., Labus, P., Schmermund, B., and Hermann, D.M. (2023). Structural changes in perineuronal nets and their perforating

GABAergic synapses precede motor coordination recovery post stroke. Journal of Biomedical Science *30*, 76.
Evans, E.L., Cuthbertson, K., Endesh, N., Rode, B., Blythe, N.M., Hyman, A.J., Hall, S.J., Gaunt, H.J., Ludlow, M.J., Foster, R.*, et al.* (2018). Yoda1 analogue (Dooku1) which antagonizes Yoda1-evoked activation of Piezo1 and aortic relaxation. Br J Pharmacol *175*, 1744-1759.
Faissner, A., and Reinhard, J. (2015). The extracellular matrix compartment of neural stem and glial progenitor cells. Glia *63*, 1330-1349.
Fawcett, J.W., Fyhn, M., Jendelova, P., Kwok, J.C.F., Ruzicka, J., and Sorg, B.A. (2022). The extracellular matrix and perineuronal nets in memory. Mol Psychiatry *27*, 3192-3203.
Gerhardt, K.J., Abrams, R.M., and Oliver, C.C. (1990). Sound environment of the fetal sheep. American Journal of Obstetrics and Gynecology *162*, 282-287.
Gottschling, C., Dzyubenko, E., Geissler, M., and Faissner, A. (2016). The Indirect Neuron-astrocyte Coculture Assay: An In Vitro Set-up for the Detailed Investigation of Neuron-glia Interactions. J Vis Exp, e54757.
Hao, Y., Stuart, T., Kowalski, M.H., Choudhary, S., Hoffman, P., Hartman, A., Srivastava, A., Molla, G., Madad, S., Fernandez-Granda, C.*, et al.* (2024). Dictionary learning for integrative, multimodal and scalable single-cell analysis. Nat Biotechnol *42*, 293-304.
Hrabetová, S., Hrabe, J., and Nicholson, C. (2003). Dead-space microdomains hinder extracellular diffusion in rat neocortex during ischemia. J Neurosci *23*, 8351-8359.
Hua, Y., Weng, L., Zhao, F., and Rambow, F. (2025). SeuratExtend: streamlining single-cell RNA-seq analysis through an integrated and intuitive framework. Gigascience *14*.
Hughes, C.S., Moggridge, S., Müller, T., Sorensen, P.H., Morin, G.B., and Krijgsveld, J. (2019). Single-pot, solid-phase-enhanced sample preparation for proteomics experiments. Nature Protocols *14*, 68-85.
Jammal Salameh, L., Bitzenhofer, S.H., Hanganu-Opatz, I.L., Dutschmann, M., and Egger, V. (2024). Blood pressure pulsations modulate central neuronal activity via mechanosensitive ion channels. Science *383*, eadk8511.
Korsunsky, I., Millard, N., Fan, J., Slowikowski, K., Zhang, F., Wei, K., Baglaenko, Y., Brenner, M., Loh, P.R., and Raychaudhuri, S. (2019). Fast, sensitive and accurate integration of single-cell data with Harmony. Nat Methods *16*, 1289-1296.
Kosnoff, J., Yu, K., Liu, C., and He, B. (2024). Transcranial focused ultrasound to V5 enhances human visual motion brain-computer interface by modulating feature-based attention. Nature Communications *15*, 4382.
Kumeta, M., Otani, M., Toyoda, M., and Yoshimura, S.H. (2025). Acoustic modulation of mechanosensitive genes and adipocyte differentiation. Communications Biology *8*, 595.
Lancaster, M.A., Renner, M., Martin, C.-A., Wenzel, D., Bicknell, L.S., Hurles, M.E., Homfray, T., Penninger, J.M., Jackson, A.P., and Knoblich, J.A. (2013). Cerebral organoids model human brain development and microcephaly. Nature *501*, 373-379.
Lewis, A.H., Cui, A.F., McDonald, M.F., and Grandl, J. (2017). Transduction of Repetitive Mechanical Stimuli by Piezo1 and Piezo2 Ion Channels. Cell reports *19*, 2572-2585.
Nikolaev, Y.A., Dosen, P.J., Laver, D.R., van Helden, D.F., and Hamill, O.P. (2015). Single mechanically-gated cation channel currents can trigger action potentials in neocortical and hippocampal pyramidal neurons. Brain Res *1608*, 1-13.

Onesto, M.M., Kim, J.-i., and Pasca, S.P. (2024). Assembloid models of cell-cell interaction to study tissue and disease biology. Cell Stem Cell *31*, 1563-1573.
Paşca, A.M., Sloan, S.A., Clarke, L.E., Tian, Y., Makinson, C.D., Huber, N., Kim, C.H., Park, J.-Y., O'Rourke, N.A., Nguyen, K.D.*, et al.* (2015). Functional cortical neurons and astrocytes from human pluripotent stem cells in 3D culture. Nature Methods *12*, 671-678.
Querleu, D., Renard, X., Versyp, F., Paris-Delrue, L., and Crèpin, G. (1988). Fetal hearing. Eur J Obstet Gynecol Reprod Biol *28*, 191-212.
Ranade, S.S., Qiu, Z., Woo, S.-H., Hur, S.S., Murthy, S.E., Cahalan, S.M., Xu, J., Mathur, J., Bandell, M., Coste, B.*, et al.* (2014). Piezo1, a mechanically activated ion channel, is required for vascular development in mice. Proceedings of the National Academy of Sciences *111*, 10347-10352.
Schneider, C.A., Rasband, W.S., and Eliceiri, K.W. (2012). NIH Image to ImageJ: 25 years of image analysis. Nature Methods *9*, 671-675.
Sloan, S.A., Darmanis, S., Huber, N., Khan, T.A., Birey, F., Caneda, C., Reimer, R., Quake, S.R., Barres, B.A., and Paşca, S.P. (2017). Human Astrocyte Maturation Captured in 3D Cerebral Cortical Spheroids Derived from Pluripotent Stem Cells. Neuron *95*, 779-790.e776.
Solis, A.G., Bielecki, P., Steach, H.R., Sharma, L., Harman, C.C.D., Yun, S., de Zoete, M.R., Warnock, J.N., To, S.D.F., York, A.G.*, et al.* (2019). Mechanosensation of cyclical force by PIEZO1 is essential for innate immunity. Nature *573*, 69-74.
Sykova, E., and Nicholson, C. (2008). Diffusion in brain extracellular space. Physiol Rev *88*, 1277-1340.
Tønnesen, J., Hrabětová, S., and Soria, F.N. (2023). Local diffusion in the extracellular space of the brain. Neurobiology of Disease *177*, 105981.
Tonnesen, J., Inavalli, V., and Nagerl, U.V. (2018). Super-Resolution Imaging of the Extracellular Space in Living Brain Tissue. Cell *172*, 1108-1121 e1115.
Tort, A.B.L., Laplagne, D.A., Draguhn, A., and Gonzalez, J. (2025). Global coordination of brain activity by the breathing cycle. Nature Reviews Neuroscience *26*, 333-353.
Trujillo, C.A., Gao, R., Negraes, P.D., Gu, J., Buchanan, J., Preissl, S., Wang, A., Wu, W., Haddad, G.G., Chaim, I.A.*, et al.* (2019). Complex Oscillatory Waves Emerging from Cortical Organoids Model Early Human Brain Network Development. Cell Stem Cell *25*, 558-569.e557.
Vince, M.A., Armitage, S.E., Baldwin, B.A., Toner, J., and Moore, B.C.J. (1982). The Sound Environment of the Foetal Sheep. Behaviour *81*, 296-315.
von Bartheld, C.S., Bahney, J., and Herculano-Houzel, S. (2016). The search for true numbers of neurons and glial cells in the human brain: A review of 150 years of cell counting. J Comp Neurol *524*, 3865-3895.
Xu, T., Zhang, Y., Li, D., Lai, C., Wang, S., and Zhang, S. (2024). Mechanosensitive Ion Channels Piezo1 and Piezo2 Mediate Motor Responses In Vivo During Transcranial Focused Ultrasound Stimulation of the Rodent Cerebral Motor Cortex. IEEE Transactions on Biomedical Engineering *71*, 2900-2910.
Zeng, W.-Z., Marshall, K.L., Min, S., Daou, I., Chapleau, M.W., Abboud, F.M., Liberles, S.D., and Patapoutian, A. (2018). PIEZOs mediate neuronal sensing of blood pressure and the baroreceptor reflex. Science *362*, 464-467.

Zhao, Q., Zhou, H., Chi, S., Wang, Y., Wang, J., Geng, J., Wu, K., Liu, W., Zhang, T., Dong, M.-Q.*, et al.* (2018). Structure and mechanogating mechanism of the Piezo1 channel. Nature *554*, 487-492.